AGU PUBLICATIONS

JGR

Journal of Geophysical Research: Oceans

RESEARCH ARTICLE

10.1002/2015JC011572

Regional influence of climate patterns on the wave climate of the southwestern Pacific: The New Zealand region

Victor A. Godoi[1], Karin R. Bryan[1], and Richard M. Gorman[2]

[1]School of Science, University of Waikato, Hamilton, New Zealand, [2]National Institute of Water and Atmospheric Research Ltd, Hamilton, New Zealand

Key Points:
- The effects of the IOD and ZW3 are critical drivers of the southwestern Pacific wave climate
- An increasing trend in wave height has been detected in the Tasman Sea
- The interface of the Pacific with the Southern Ocean causes contrasting wave climates in New Zealand

Correspondence to:
V. Godoi,
victorgodoirj@gmail.com

Citation:
Godoi, V. A., K. R. Bryan, and R. M. Gorman (2016), Regional influence of climate patterns on the wave climate of the southwestern Pacific: The New Zealand region, *J. Geophys. Res. Oceans*, *121*, doi:10.1002/2015JC011572.

Received 17 DEC 2015
Accepted 11 MAY 2016
Accepted article online 17 MAY 2016

Abstract This work investigates how the wave climate around New Zealand and the southwest Pacific is modulated by the Pacific Decadal Oscillation (PDO), El Niño-Southern Oscillation (ENSO), Indian Ocean Dipole (IOD), Zonal Wave-number-3 Pattern (ZW3), and Southern Annular Mode (SAM) during the period 1958–2001. Their respective climate indices were correlated with modeled mean wave parameters extracted from a 45 year (1957–2002) wave hindcast carried out with the WAVEWATCH III model using the wind and ice fields from the ERA-40 reanalysis project. The correlation was performed using the Pearson's correlation coefficient and the wavelet spectral analysis. Prior to that, mean annual and interannual variabilities and trends in significant wave height (H_s) were computed over 44 years (1958–2001). In general, higher annual and interannual variabilities were found along the coastline, in regions dominated by local winds. An increasing trend in H_s was found around the country, with values varying between 1 and 6 cm/decade at the shoreline. The greatest H_s trends were identified to the south of 48°S, suggesting a relationship with the positive trend in the SAM. Seasonal to decadal time scales of the SAM strongly influenced wave parameters throughout the period analyzed. In addition, larger waves were observed during extreme ENSO and IOD events at interannual time scale, while they were more evident at seasonal and intraseasonal time scales in the correlations with the ZW3. Negative phases of the ZW3 and ENSO and positive phases of the IOD, PDO, and SAM resulted in larger waves around most parts of New Zealand.

1. Introduction

Wave dynamics have a significant impact on human lives, particularly in island nations such as New Zealand. A wide variety of recreation, fishing and trade activities at sea require constant monitoring of sea state. In nations with less established roading and rail networks, people rely on shipping trade between cities and depend on wave conditions to do so. Recently, waves have also been used as energy resource to supply power to coastal communities. Engineering specifications for coastal and offshore structures, for instance, harbors and oil platforms, require a detailed understanding of wave conditions at building sites. The synthesis of wave conditions, based on long-term statistics, is scientifically known as "wave climate" [*Sterl and Caires*, 2005], and has been required for many purposes in addition to construction, such as evaluation of extreme wave heights, planning of naval and marine operations [*Cox and Swail*, 2001], wave energy estimation, and oil spills and sediment transport assessments. Amongst the information that a wave climatology provides, of particular interest is the relationship between atmospheric oscillation modes and the wave climate of a region, since these patterns can allow us to understand future trends in the nature of coastal hazards and may serve as proxies to understand potential effects of future climate change [*Quan et al.*, 2013].

Atmospheric oscillation modes can dramatically alter weather conditions and, as a consequence, the wave conditions. Some climate patterns have been shown to be influential on local scales, while others are known to impact on a wide range of regions [e.g., *Hemer et al.*, 2010; *Harley et al.*, 2010; *Gorman et al.*, 2003b], and these are often called "teleconnection" phenomena. Significant attention has been devoted to the impacts caused by climate patterns on ocean waves, especially in regions where severe storms play an important role. Despite being located in a relatively isolated portion of the world, New Zealand is a particularly interesting case because it lies at the interface of the Southern and Pacific oceans and the Tasman Sea, and hence is influenced by a range of climatic drivers. The Southern Ocean has also been proven to be

extremely important for regulating climate. By sinking and storing carbon dioxide and heat in deep waters, the Southern Ocean slows down global warming, minimizing anthropogenic impacts [*Lavergne et al*., 2014; *Sallée et al*., 2012; *Russell et al*., 2006]. Therefore, there is general interest in the impact of climate oscillations on the properties of the Southern Ocean, and New Zealand plays a key role in controlling these properties [*Chiswell et al*., 2015; *Morris et al*., 2001] by changing the ocean dynamics in the area (e.g., by blocking and steering the flow) and influencing waves, currents, and sea level. As a consequence, phenomena of global scales are directly affected by changes in the waters surrounding New Zealand [*Sasaki et al*., 2008; *Davis*, 2005].

New Zealand's high-latitude location along with the long stretch of ocean lying immediately to the west of it provide a highly energetic wave environment [*Gorman et al*., 2003b]. Swell waves generated in the region just south of the country propagate through the Pacific Ocean and hit the west coasts of South America, Central America, and part of the North America [*Young*, 1999]. The long period of these swells and their seasonality are different from other more well-studied areas, such as the North Atlantic, and so a greater understanding is essential for hazard management along South Pacific shipping routes, oil exploration, coastal engineering, and wave power generation. Estimates show substantial wave power potential to the New Zealand region [*Rusu and Guedes Soares*, 2009]. Moreover, the Trans-Pacific Partnership will have a direct impact on trade of goods across the Pacific [*World Bank Group*, 2016], which will affect not only the 12 countries involved in the agreement, but also their trade partners, and thus increase pressure on south Pacific shipping routes.

Different methodologies have been applied to assess the wave climate around New Zealand. *Pickrill and Mitchell* [1979] used approximately 40 sources of data, including deep water, mid-water, and shore-based visual and buoy observations, covering approximately 17 years. *Laing* [1993] implemented a second-generation wave model to perform a 5 month wave hindcast for the New Zealand region, which covered mainly the winter of 1989. Later on, *Laing* [2000] used approximately 13 years (1985–1998) of wave data derived from radar altimeters to create a wave climatology for the New Zealand waters. The coastal wave climate was assessed again in more detail by *Gorman et al*. [2003a,b]. The authors conducted a 20 year (1979–1998) deep water wave hindcast and extracted boundary conditions from it to use as initial conditions for a shallow-water hindcast. All these authors found similar spatial patterns of significant wave height (H_s), where the south coast receives the highest energy waves, followed by the west, east, and north coasts, respectively. *Pickrill and Mitchell* [1979] observed that the westerly air flow is responsible for generating the waves that hit the south coast. Swell waves generated to the south also reach the east coast, which in turn, receives in addition locally generated northerly and southerly storm waves. The west coast receives southerly swells and locally generated westerly and southerly storm waves. Finally, the north coast is dominated by northeasterly waves. Some of the most intense storm conditions were observed to occur in the summer months as a result of tropical cyclones [*Gorman et al*., 2003a]. Increasing wave heights off the northeast coast of the North Island occur during La Niña events [*Gorman et al*., 2003b]. In contrast, the rest of the country experiences increasing wave heights during El Niño events [*Gorman et al*., 2003b]. *Laing* [1993] also verified that monthly anomalies of mean H_s seem to be associated with El Niño events in winter.

Extreme wave heights in southern Pacific, especially in the New Zealand region, are modulated by positive phases of the Antarctic Oscillation and Indian Ocean Dipole [*Izaguirre et al*., 2011]. According to *Caires et al*. [2006], significant increases of extreme H_s are expected around the southern half of New Zealand in the austral winter. On the basis of the 20 year hindcast produced by *Gorman et al*. [2003a], *Stephens and Gorman* [2006] estimated extreme H_s for the New Zealand region. The authors showed that the estimates follow the trend of the mean H_s, although they present less spatial variation. The smallest extreme H_s value (13.9 m) was observed in the northeast, and the largest (19.3 m) in the southwest.

In summary, preliminary studies have shown that the wave climate in the southwest Pacific is influenced by the state of climatic indicators, and the response around New Zealand is spatially variable [*Godoi et al*., 2015], depending on the exposure of the coastline to generating regions. This paper extends on this previous work by describing the nature of the correlation, determining its time scale, and how these changes depend on the local exposure of the coastline. In order to determine how atmospheric oscillations modulate the regional wave climate around New Zealand, mean wave parameters generated by a 45 year wave hindcast were used to conduct three main analyses. First, mean annual and interannual variabilities were

calculated to provide an indication of the most vulnerable areas to climate change around the country. Then, time series of mean wave parameters were correlated with climate indices using a basic statistical tool, the Pearson's correlation coefficient, and a more sophisticated technique based on spectral energy, the wavelet analysis. The long time frame of the analysis allows us to capture some of the longer time scale patterns and how these differ depending on exposure to the Southern Ocean in contrast to the South Pacific Ocean.

The paper is organized as follows. The climate patterns that potentially influence the wave climate of New Zealand are briefly described in section 2. Details of the wave hindcast carried out to conduct the analyses are explained in section 3. Section 4 addresses the manipulation of the data set used in the methodology of this study, which in turn is explained along with the discussion of the results in sections 5 and 6. Finally, the conclusions are presented in section 7.

2. Atmospheric Oscillation Modes

A number of atmospheric oscillation modes have been described in the literature, and at least five of them have been reported to somehow affect the weather and/or the ocean in the southwest Pacific. These are the Pacific Decadal Oscillation (PDO), the El Niño-Southern Oscillation (ENSO), the Indian Ocean Dipole (IOD), the Zonal Wave-number-3 Pattern (ZW3), and the Antarctic Oscillation (AAO), frequently called Southern Annular Mode (SAM) [*Limpasuvan and Hartmann*, 1999] (refer to Table A1 in Appendix A for a summary of acronyms used here and throughout the text).

The PDO is an interdecadal climate fluctuation identified by the leading empirical orthogonal function of monthly sea surface temperature (SST) anomalies over the North Pacific [*Mantua et al*., 1997; *Taylor et al*., 2009; *Deser et al*., 2010]. Only two cycles have been verified within the last century, with predominantly negative SST anomaly between 1947 and 1976, and predominantly positive SST anomaly between 1925 and 1946, and after 1977 [*Mantua et al*., 1997].

Like the PDO, the ENSO is also characterized by SST anomalies [*Zhang et al*., 1997]. Its signatures are primarily observed over the equatorial region of the Pacific Ocean with interannual cycles that range from 2 to 7 years [*Trenberth and Hurrell*, 1994; *Cane*, 2005; *Stopa et al*., 2013]. The ENSO has been recognized by its teleconnection effects or its influence on conditions all over the world as a result of the so-called "Atmospheric Bridge" [*Alexander et al*., 2002]. The ENSO is measured by the Southern Oscillation Index (SOI) [*Ropelewski and Jones*, 1987], which is the difference between the Darwin and Tahiti surface air pressures.

An interannual variability with dipole-shaped signature in the SST field over the tropical Indian Ocean defines the IOD [*Saji et al*., 1999; *Izumo et al*., 2010]. This oscillation is measured by the Dipole Mode Index (DMI), which describes the difference in SST anomaly between the tropical western Indian Ocean and the tropical southeastern Indian Ocean. Extreme IOD events occurred in 1961, 1994, and 1997 [*Cai et al*., 2014; *Saji et al*., 1999], and despite its irregular cycle, the IOD seems to have strong cycles with periodicities of approximately 2 [*Webster et al*., 1999] and 5 years [*Webster et al*., 1999; *Yuan and Cao*, 2013].

The ZW3 is a quasi-stationary planetary wave-number-3 pattern that significantly impacts on daily [*Kidson*, 1988], seasonal [*Mo and White*, 1985], and interannual [*Trenberth*, 1980; *Karoly*, 1989; *Cai et al*., 1999] time scales at midlatitudes of the Southern Hemisphere [*van Loon and Jenne*, 1972; *Raphael*, 2004]. It is normally identified by sea ice, sea level pressure (SLP), wind [*Yuan and Li*, 2008], and geopotential height fields [*Mo and White*, 1985]. Indices for the ZW3 have been computed by different authors [e.g., *Mo and White*, 1985; *Raphael*, 2004] using mainly SLP and geopotential height values at three selected geographical points, which vary in accordance with the methodology adopted by each author.

Zonally symmetric anomalies of opposite signs in Antarctica and the midlatitudes of the Southern Hemisphere define the SAM [*Marshall*, 2003]. Such anomalies can be identified in several atmospheric fields, such as surface pressure and surface temperature, and they modulate phenomena at time scales that vary from high to low frequency. Noteworthy cycles of 2.7, 4.2, and 45.7 months were reported by *Gong and Wang* [1999], who defined an index to represent the SAM. The index is called Antarctic Oscillation Index (AOI) or Southern Annular Mode Index (SAMI), and measures the difference of zonal mean sea level pressure between 40°S and 65°S.

3. Wave Model Hindcast

A 45 year wave hindcast (September/1957 to August/2002), hereinafter 45WH, has been carried out using the WAVEWATCH III v. 3.14 model [*Tolman*, 2009]. This is a third-generation wave model that solves the wave action density spectrum as a function of wavenumber and direction. Parameterizations of physical processes include wave growth and decay by wind stress, nonlinear resonant interactions, bottom friction, dissipation by white capping, surf breaking, and scattering by wave-bottom interactions [*Tolman*, 2009]. Refraction and straining of the wavefield due to spatial variations of the mean water depth are included in the shallow-water governing equation.

In order to perform the simulation, 1 min bathymetric results from the ETOPO1 1 arc min global relief model [*Amante and Eakins*, 2009] were implemented in the wave model to assign depths to oceans and seas, and delimit borders of continents, countries, and islands. The ETOPO1 was developed by the National Geophysical Data Center (NGDC) and is aimed at supporting tsunami forecasting, modeling, and warning, and also ocean circulation modeling. Wind fields at 10 m and ice fields from the ERA-40 reanalysis data set [*Uppala et al*., 2005] were employed as boundary conditions in the 45WH. The ERA-40 was created by the European Centre for Medium-Range Weather Forecasts (ECMWF) and spans 45 years, from September 1957 to August 2002. It was produced by assimilating atmospheric and oceanographic observations from different sources, such as aircrafts, ocean buoys, ships, radiosondes, balloons, satellite-borne instruments, and surface platforms. The ERA-40 products used in the 45WH have temporal resolution of 6 h and spatial resolution of 1.125°.

The evolution of the directional wave spectrum was computed by using 2 one-way nested numerical grids (Figure 1) with 25 logarithmically spaced frequencies and 24 equally spaced directions. The global grid covers latitudes 81°S–81°N and longitudes 0°E–358.875°E at 1.125° resolution, while the regional grid has spatial resolution of 0.125° in longitude and 0.09375° in latitude, and covers latitudes 51.75°S–32.625°S and longitudes 162°E–185.625°E. The bottom friction was represented by the Joint North Sea Wave Project (JONSWAP) parameterization [*Hasselmann et al*., 1973], and the *Cavaleri and Malanotte-Rizzoli* [1981] formulation assisted the improvement of the initial wave growth behavior from calm conditions. The formulation proposed by *Tolman and Chalikov* [1996] was used to compute input and dissipation terms, whereas the discrete interaction approximation (DIA) [*Hasselmann et al*., 1985] was used in modeling nonlinear wave-wave interactions. Wind and ice fields were input every 6 h, and the output parameters were generated at 3 and 1 h intervals for the global and regional domains, respectively.

The 45WH has been validated with buoy and satellite measurements. Buoy records from the National Data Buoy Center (NDBC) and from stations around New Zealand (see Figure 1 for buoy locations) have been used to verify the accuracy of the hindcast. Several wave parameters were validated, these were significant wave height, mean wave direction, directional spread, peak wave period, peak wave direction, and mean wave period (second moment), depending on what was available from each wave buoy. The statistical indices computed in the validation were the mean, standard deviation, bias, root-mean-square error (RMSE), scatter index, and correlation coefficient. Satellite altimetry data in the New Zealand region were obtained from the TOPEX/Poseidon, ERS1 and ERS2 missions, and subject to a set of

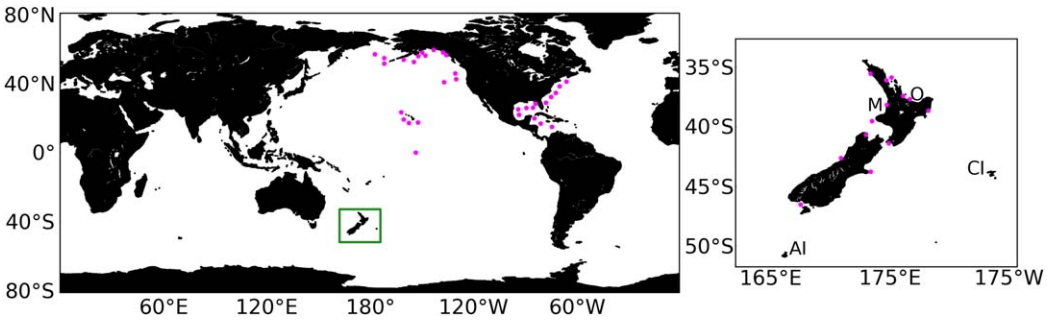

Figure 1. Grid domains used in the 45 year wave hindcast. (left) Global domain. The area delineated by the green square represents the regional domain, which is expanded in the right plot. AI, CI, M, and O stand for Auckland Islands, Chatham Islands, Mokau, and Ohiwa, respectively, mentioned later in the text. Pink dots represent the sites of the buoys used for validating the hindcast.

quality control procedures as detailed by *Laing* [2000] and summarized by *Gorman et al*. [2003b]. First, the whole hindcast domain was divided into areas of 2.25° × 2.25° for both satellite altimetry data and model results. Then, occurrence distributions of H_s within each of these bins were computed and compared over the available time period. Additionally, comparisons between altimetry data and global model results were performed by calculating H_s monthly means for all the values within each bin.

In general, modeled results agreed satisfactorily with both buoy and satellite measurements. As a result of the reasonably low spatial-temporal resolution of wind fields, which does not account for significantly strong velocity gradients and sudden changes in the wind direction, mean wave parameters were generally underestimated during extreme events. Despite this, the 45WH results are suitable for the purpose of the present work, since monthly averages have been used (as described in the next section) and results have been generated for a considerably long time period. Due to the coarse spatial resolution near the coast, the global hindcast presented better results at the NDBC buoys than at the New Zealand buoys. The RMSE from comparisons of measured and modeled H_s had values of 0.52 m, averaged over the NDBC buoys, and 0.61 m averaged over the New Zealand buoys, while the correlation coefficient from the same comparisons averaged 0.89 and 0.83 over the NDBC and New Zealand buoys, respectively. In the comparison with satellite data, the hindcast results underestimated H_s (with up to 0.5 m of negative bias) in the western Tasman Sea and near the New Zealand coast, while overestimation (with localized positive bias of order 0.5 m) was seen in the Southern Ocean. The latter was particularly more pronounced during the austral winter. Significant improvement was observed in the comparisons between the regional results and New Zealand buoy data, with mean RMSE of 0.50 m, and mean correlation of 0.83, obtained from H_s comparisons. Comparisons of the regional hindcast with satellite data showed a reduction in the magnitude of negative biases in the wave height near the New Zealand coast seen in the global hindcast. Additional details on the 45WH and its validation can be found in *Gorman et al*. [2010].

4. Data Preparation

An overview of the wave climate can be obtained by computing monthly means over a long period of time. Monthly means of significant wave height (H_s), peak wave period (T_p), mean wave period (T_{mean}), and peak wave direction (D_p) were calculated over 44 years (1958–2001). Only the full calendar years covered by the 45WH were considered in the analysis, disregarding the years 1957 and 2002 due to incomplete data coverage.

According to *Stopa et al*. [2013], atmospheric oscillations have a more significant impact on extreme than on average conditions. Extreme conditions have distinct definitions depending on the author. *Storlazzi et al*. [2015], for example, define extreme significant wave height as the mean of the top 5% H_s within a specific period. On the other hand, *Stopa et al*. [2013] and *Bosserelle et al*. [2012] use the mean of the top 10% H_s. Here we use the ninetieth percentile as the threshold for determining monthly extreme significant wave heights ($90thH_s$) for the 44 year period.

The five wave parameters used in this work enable a comprehensive understanding of the wave climate around New Zealand. The wave period and wave direction associated with the most energetic waves are represented by T_p and D_p, respectively, while $90thH_s$ takes into consideration wave heights of extreme events (H_s and T_{mean} are more representative of mean wave conditions of the ocean).

Monthly means of the SOI, DMI, SAMI, PDO index, and ZW3 index were sourced from the National Oceanic and Atmospheric Administration (NOAA), Japan Agency for Marine-Earth Science and Technology (JAMSTEC), British Antarctic Survey (BAS), Japan Meteorological Agency (JMA), and *Raphael* [2004], respectively. The ZW3 index is only available from 1979 on, whereas the other indices cover the whole hindcast period. The anomalies of the climate indices were computed by simply subtracting overall mean from the monthly means. The same was done for the wave parameters in order to investigate how they are modulated by the climate modes.

5. Significant Wave Height Variability

The mean annual variability (MAV) and interannual variability (IAV) of H_s were computed for each grid point of the regional domain over the 44 year period following the methodology described in *Stopa et al*. [2013].

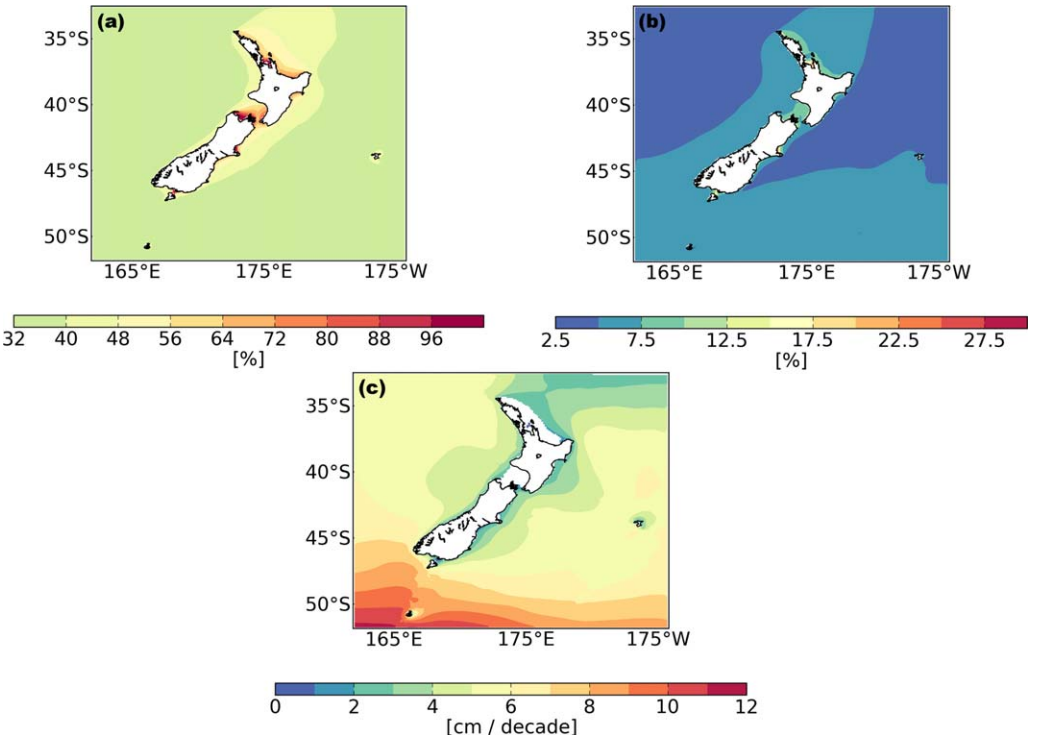

Figure 2. (a) Mean annual variability (MAV) of significant wave height; (b) interannual variability (IAV) of significant wave height; (c) 44 year (1958–2001) trend in significant wave height (only statistically significant values at the 95% confidence level are plotted). Note that the color scales are different to better represent the parameters.

The MAV (equation (1)) is defined as the average of the annual standard deviation normalized by the annual average, and the IAV (equation (2)) is determined by the standard deviation of the annual means normalized by the overall mean [*Stopa et al*., 2013]. Thus, MAV and IAV can be written as:

$$MAV = \frac{1}{m}\sum_{j=1}^{m}\sqrt{\frac{1}{n}\sum_{k=1}^{n}\left[x_{jk}-\left(\frac{1}{n}\sum_{k=1}^{n}x_{jk}\right)\right]^2}\left(\frac{1}{n}\sum_{k=1}^{n}x_{jk}\right)^{-1} \tag{1}$$

$$IAV = \sqrt{\frac{1}{m}\sum_{j=1}^{m}\left\{\left(\frac{1}{n}\sum_{k=1}^{n}x_{jk}\right)-\left[\frac{1}{m}\sum_{j=1}^{m}\left(\frac{1}{n}\sum_{k=1}^{n}x_{jk}\right)\right]\right\}^2}\left(\frac{1}{nm}\sum_{j=1}^{m}\sum_{k=1}^{n}x_{jk}\right)^{-1} \tag{2}$$

where x is the time series of significant wave height over a period of m years with n records each, and j and k refer to the year and record, respectively.

Signatures of the wave climate of New Zealand can be clearly noted in the MAV and IAV maps (Figures 2a and 2b). Relatively large variability is observed in coastal areas, especially in sheltered regions dominated by locally generated waves, such as to the north of both islands. This characteristic agrees with the works by *Stopa et al*. [2013] and *Bosserelle et al*. [2012], who conducted their studies for the whole globe and Western Australia, respectively. The large values in northerly exposed regions are a consequence of the absence of steady southerly swells. The northern area experiences tropical cyclones, typically in summer, which probably contributes to relatively large MAV in that region (Figure 2a). As reported by *Laing* [2000], there is a larger difference between the mean and 99.9 percentile values to the north of the country, resulting in relatively large variability. The same northern region as well as the areas off the west and south coasts show higher IAV than off the east coast region (Figure 2b), suggesting a stronger association of those areas with atmospheric oscillations that are characterized by interannual cycles. As previously mentioned, *Gorman et al*. [2003b] reported increasing wave heights off the northeast coast of the North Island during positive phases of the ENSO, and around the rest of the country during negative phases, especially off the southwest and south regions. In contrast to the IAV, the high frequency of southwesterly swells with nearly constant

wave height in the west coast results in smaller MAV (Figure 2a) at this coast in comparison to the east coast. Regarding deep water regions, the area to the south of 45°S generally has larger IAV than most regions to the north of this parallel (Figure 2b), which indicates a possible relation with the SAM. As cited by *Marshall* [2003] and *Kushner et al*. [2001], a trend toward the positive phase of the SAM has been detected by several works, leading to strengthening of westerly winds in the Southern Ocean. Finally, the fluctuations of H_s throughout the seasons produce generally higher values in the MAV than in the IAV, highlighting the prevalence of high-frequency oscillations in the wave climate variability.

To complement the MAV and IAV results, the trend in H_s was computed for the period 1958–2001 (Figure 2c). This was carried out by fitting a linear curve to H_s monthly means on each grid point of the regional domain using the least squares regression. Only statistically significant values at the 95% confidence levels are displayed, which excludes the regions immediately to the north of both islands where the largest MAV is found. The whole regional domain presents an increasing trend in H_s. The areas adjacent to the coastline have a positive trend that varies from values smaller than 1 cm/decade, in more sheltered sites, to 6 cm/decade in the southwest coast. The greatest trends, of up to 12 cm/decade, are observed to the south of 48°S, suggesting a relationship with the positive trend in the SAM. These results are consistent with the general trend of increasing H_s found by *Coggins et al*. [2015]. Nevertheless, their results are more focused on offshore regions due to the coarser spatial and temporal resolutions in relation to the present data set.

6. Relationship Between the Wave Parameters and the Climate Patterns

6.1. Correlation Analysis

Monthly mean anomalies of H_s, T_{mean}, T_p, and D_p fields and anomalies of $90thH_s$ fields were correlated with monthly mean anomaly time series of the SOI, SAMI, DMI, PDO index, and ZW3 index by computing the Pearson's correlation coefficient (R) for each grid point of the 45WH regional domain (Figures 3 and 4). The 95% confidence levels were used to determine statistically significant results, and are represented by shaded light gray in Figures 3 and 4. The R values mentioned throughout the discussion refer to the highest statistically significant values found for each climate index. In view of the fact that all those atmospheric oscillations were derived from linear analyses, climate anomalies associated with cool phases are simply the opposites of those for warm phases [*Mantua and Hare*, 2002].

The SAM is the prevailing mode to the south of New Zealand ($R = 0.28$ for H_s; $R = 0.24$ for $90thH_s$; $R = 0.36$ for T_{mean}, which actually reaches its maximum in the Chatham Islands ($R = 0.45$); and $R = 0.45$ for T_p). The intensification of the SAM over recent decades, a trend to the positive phase of the SAMI, leads to a strengthening of the circumpolar westerlies [*Schott et al*., 2009; *Marshall*, 2003; *Hemer*, 2010; *Gillett and Thompson*, 2003] which results in larger wave heights [*Hemer et al*., 2010; *Bosserelle et al*., 2012] and, as suggested by the R values, larger wave periods (Figure 3). This trend has been occurring since the mid-1960s [*Marshall*, 2003] accompanied by a reduction in the number of cyclones south of 40°S, with greatest reductions near 60°S [*Simmonds and Keay*, 2000]. Associated with such reductions are increases in intensity of cyclones to the south of Australia, in the Tasman Sea, and in the central Pacific, and decreases in the eastern Pacific and eastern Indian oceans [*Simmonds and Keay*, 2000]. Moreover, a poleward shift of the extratropical cyclone storm tracks has also been observed as a result of the positive trend [*Gillett and Thompson*, 2003]. *Hemer et al*. [2010] reported a trend of counterclockwise rotation of wave direction south of ~48°S during positive phases of the SAM. In contrast to this trend, one sees a clockwise rotation of D_p associated with positive anomalies of the SAMI in our results (Figure 3), which is represented by positive correlations. On the other hand, a counterclockwise rotation of D_p, represented by negative correlations, is observed along and off the west and north coasts during positive phases of the SAM. A substantial component of the variance of the wave parameters is explained by the SAM in most parts of the regional domain for D_p, T_p, and T_{mean}, to the east of New Zealand for H_s and along the west coast for H_s and $90thH_s$. In the case of T_p and T_{mean}, correlations indicate that higher wave periods are modulated by increasing values of the SAMI.

Negative correlations of the SOI with H_s and $90thH_s$ ($R = -0.22$ in southern New Zealand) are found around the country, except to the north (Figure 3). This is in agreement with the works by *Gorman et al*. [2003b] and *Laing* [2000], who observed increased occurrence of southwesterly winds around New Zealand during negative ENSO phases (El Niño). Accompanying increasing wave heights during El Niño events are increasing wave periods, as illustrated by negative correlations. During La Niña events (positive phases of the

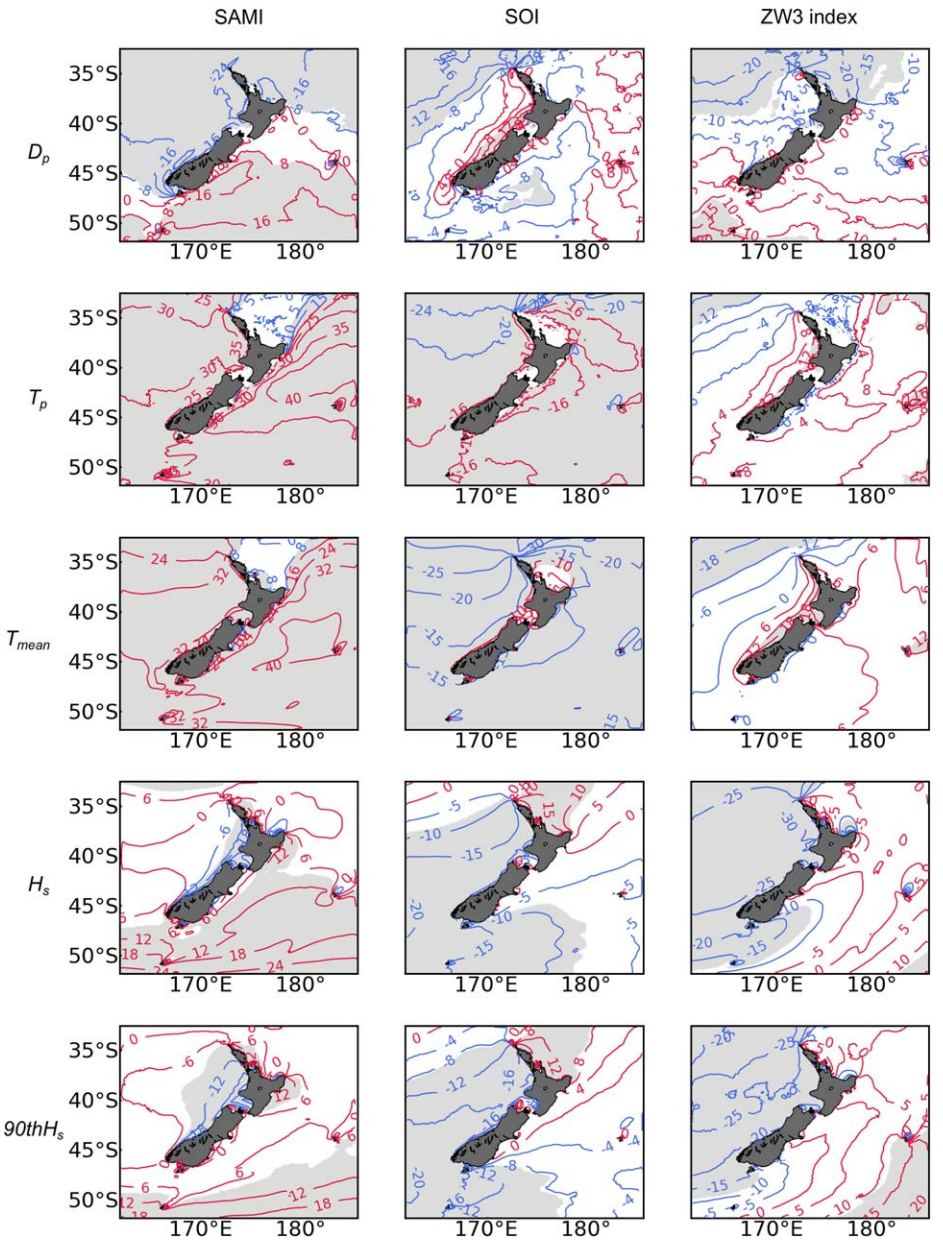

Figure 3. Correlation coefficients (in percentage) of the (first column) SAMI and (second column) SOI with the wave parameters (rows) for the period 1958–2001. Correlations of the wave parameters with the (third column) ZW3 index comprise the period 1979–2001. Red/blue contours represent positive/negative correlations. Statistically significance within 95% is represented by light gray color.

ENSO), increased occurrence of northeasterly winds in the northeast coast have been noted [*Gordon*, 1986; *Gorman et al*., 2003b], possibly as a result of an increasing number of cyclones in Australasia during such events [*Sinclair et al.* 1997]. Larger wave heights with smaller wave periods are observed to the north of New Zealand as a consequence of La Niña events. Both H_s and $90thH_s$ are positively correlated ($R = 0.22$) with the SOI, while T_{mean} and T_p are negatively correlated ($R = -0.37$). A possible explanation for the inverse relationship between increasing wave heights and decreasing wave periods would be the formation of smaller wave fetches resulting from storms that track more closely to the shore during cold ENSO conditions than during warm and neutral ENSO conditions. This explanation agrees with *Revell and Goulter* [1986], who verified that the origin points of tropical cyclones tend to be concentrated farther to the northeast with decreasing SOI. According to *Hemer et al*. [2010], there is a clockwise/counterclockwise rotation of wave direction in the Tasman Sea and in the Western Pacific Ocean during El Niño/La Niña events. In other words, since wave direction is predominantly southeasterly during both phases of the ENSO [*Hemer et al*.,

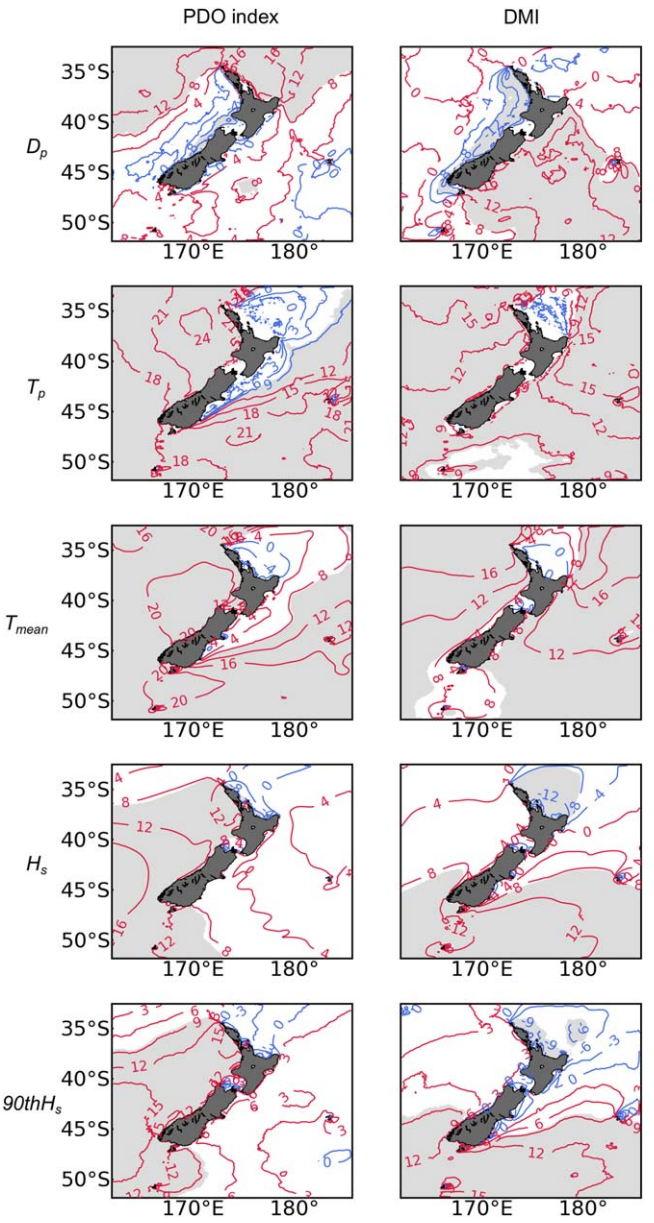

Figure 4. Correlation coefficients (in percentage) of the PDO index and DMI (columns) with the wave parameters (rows) for the period 1958–2001. Red/blue contours represent positive/negative correlations. Statistically significance within 95% is represented by light gray color.

2010], southerly/easterly waves are more common during El Niño/La Niña events. Most areas around New Zealand show no statistically significant relationship between SOI and D_p. However, the rotation of wave direction noted by *Hemer et al.* [2010] agrees with our results in two of three regions where statistically significant results occur. Negative correlations are present in the northwestern area of the regional domain and off the southeast coast of the South Island. On the other hand, the region adjacent to the west coasts of both North and South Islands shows positively correlated values, in opposition to the study by *Hemer et al.* [2010]. This difference might be related to the products used by the authors for generating their results. Satellite observations are of limited application to coastal waters as a result of the influence of land on the return signal [*Gorman et al.*, 2003a]. In addition, the spatial resolutions of both satellite observations and model results used by *Hemer et al.* [2010] are coarser than the one used here, hampering a high-quality representation of coastal regions.

In the atmospheric circulation, the ridges of the planetary ZW3 wave have preferred locations of formation; these are over southern South America, southern Indian Ocean, and southwest of New Zealand [*Raphael*, 2004; *Garreaud and Battisti*, 1999; *Yuan et al.*, 1999]. Consequently, preferred locations for cyclogenesis are observed in the open ocean north of the ice cover [*Yuan and Li*, 2008]. Negative correlations (Figure 3) of the ZW3 with H_s ($R = -0.32$), $90thH_s$ ($R = -0.27$), and D_p ($R = -0.27$) are consistent with the zonal flow associated with negative phases of the ZW3. Conversely, the northward wind stress anomaly between southwest Australia and south of New Zealand [*Cai et al.*, 1999] suggests that smaller waves with a counterclockwise rotation hit the study area during positive phases of the ZW3. Strong meridional flow is associated with positive phases of the ZW3, and is more pronounced from Australia to South America [*Raphael*, 2004] due to the troughing of the ZW3 wave (generated by the presence of a low-pressure system) over the south Pacific. Positive correlations of T_{mean} ($R = 0.31$) and T_p ($R = 0.24$) with the ZW3 index indicate increasing wave periods as a result of the meridional flow, but they are statistically significant only along the west coast of New Zealand.

The PDO is not the most influential mode on any wave parameter around New Zealand. However, considerable positive correlations with T_{mean} ($R = 0.24$) and T_p ($R = 0.25$) are found to the west of the country (Figure 4). According to *Mantua et al.* [1997], the SOI is correlated with the PDO index, such that positive PDO

tends to coincide with El Niño-like conditions. This explains increasing wave periods as well as increasing wave heights ($R = 0.19$ for H_s; and $R = 0.18$ for $90thH_s$) around the country, excepting to the north, during positive phases of the PDO. However, the correlations of wave height with the PDO index are statistically significant only to the west and in southern New Zealand. Despite not being statistically significant, the negative correlations of wave height and wave periods with the PDO index to the north of the country are consistent with negative phases of the PDO, in which La Niña-like conditions are expected to occur in the region. Regarding the wave direction, statistically significance is found only to the north ($R = 0.24$) and in part off the west coast of the country, and exhibits a clockwise rotation pattern during positive phases of the PDO.

Like the PDO, the IOD is not the most influential mode on any wave parameter around New Zealand, presenting maxima absolute correlation values (Figure 4) equal to $R = 0.19$ (for T_{mean}, T_p, and D_p; and smaller for others). According to *Schott et al*. [2009], the IOD can either self-generate or be externally triggered by the ENSO. The opposite is also true, with the positive phase of the IOD often preceding positive phases of the ENSO [*Izumo et al*., 2010]. Signals of the IOD influencing the zonal winds over the Pacific Ocean were described by *Izumo et al*. [2010]. This means that indirect effects of the IOD can take place through the effect of the ENSO, since the modes are correlated. The IOD is weak in most years [*Schott et al*., 2009], presenting anticyclonic circulation at low levels during its positive phase [*Yuan and Cao*, 2013], easterly winds along the equator [*Cai et al*., 2014; *Webster et al*., 1999; *Yuan and Cao*, 2013], where weak westerlies normally prevail [*Cai et al*., 2014; *Webster et al*., 1999], and westerly flow near 30°S [*Cai et al*., 2014]. The most energetic waves of the world occur in the Southern Ocean between South Africa and Australia [*Young*, 1999], where the influence of the IOD is rarely addressed. Such energetic waves mainly hit the west and south coasts of New Zealand as they propagate from the Indian Ocean to the South Pacific Ocean. Positive correlations of the DMI with T_{mean}, T_p, H_s, and $90thH_s$ are found in most parts of the regional domain (Figure 4), which agree with the study of *Izaguirre et al*. [2011], who observed increasing extreme wave height in the southwestern Pacific during IOD positive phases. Negative correlations are found to the north of New Zealand for H_s and $90thH_s$, indicating decreases in the wave height during positive IOD phases and vice versa. A counterclockwise rotation of D_p is seen along the west coast of the country, while a reverse pattern is observed to the east.

6.2. Cluster and Wavelet Analyses

According to *Bell et al*. [2000] and *Goring and Bell* [1999], quasiperiodic fluctuations that vary in both the magnitude and the time scale, such as those under consideration here, require an analysis that is different from the traditional Fourier spectral analysis which assumes stationarity. The wavelet technique has been used as an alternative for resolving nonstationary dominant modes of variability [*Goring and Bell*, 1999; *Grinsted et al*., 2004]. The wavelet power spectrum provides an indication of periods of time that most contribute to the dominant cycles, and is obtained by taking the average of the square of the wavelet coefficients. The relationship between two variables is identified by the wavelet coherence spectrum.

To facilitate the wavelet spectral analysis, a subset of geographical locations was selected for examination. The selection was based on a cluster analysis conducted to divide the 45WH regional domain into subregions that encompass areas with similar wave climate. *Pickrill and Mitchell* [1979] identified four main wave climates around New Zealand. In order to be consistent with them, four clusters were employed, each one being representative of each subregion (wave climate). Attempts using five and more clusters were also performed, but no significant gain in information was obtained. Forty-four years (1958–2001) of mean fields of H_s and T_{mean} were standardized to a Gaussian distribution (zero mean and unit variance) for the cluster analysis. The clustering was based on the *k*-means algorithm [*Hartigan and Wong*, 1979; *Kanungo et al*., 2002; *Likas et al*., 2003], which was executed 10 times with different initial centroid seeds using 300 iterations for each run.

The results of the cluster analysis (Figure 5a) seem to represent fairly well the spatial distribution of the four main wave climates described by *Pickrill and Mitchell* [1979]. Interesting features of the 44 year average of significant wave height (Figure 5b) can be observed in the cluster analysis results. First, areas with distinct wave climates are clearly demarcated by each color, roughly representing the four quadrants. Southwesterly swells propagate not only along the west coast of both islands but also along the south coast of the South Island. The shadowing to the north of the northern portion of New Zealand clearly shows the obstruction caused by the presence of landmasses, which prevent energetic southwesterly waves from reaching that region and consequently result in a less rough wave climate. The same occurs to the north of Chatham and Auckland Islands,

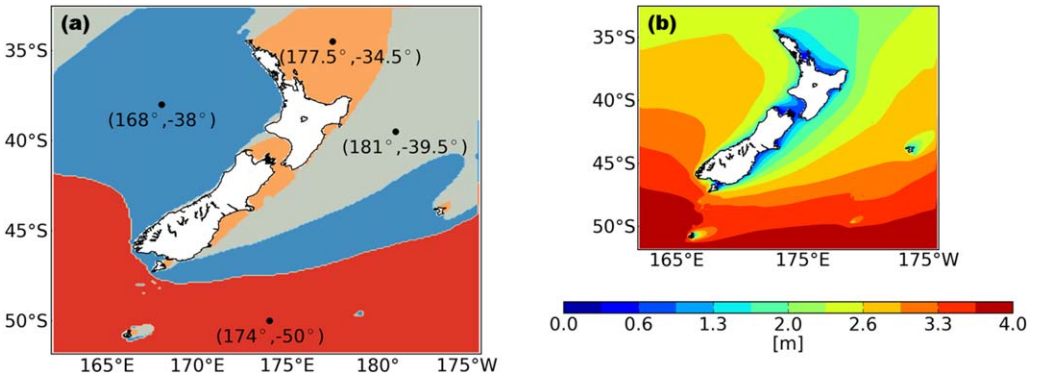

Figure 5. (a) Results of the cluster analysis. Each color represents one cluster. The black dots represent the geographical coordinates where time series of the wave parameters were extracted to be used in the wavelet analysis; (b) 44 year (1958–2001) average of significant wave height.

located near the 45°S and 50°S parallels, respectively. Finally, the sectors immediately seaward of the east coast and between the North and South Islands present a relatively moderate wave climate.

Anomalies of the wave parameters were computed for the monthly time series extracted from the central geographical coordinate of each cluster (henceforth cluster), whose positions are 181°E/39.5°S, 177.5°E/34.5°S, 168°E/38°S, and 174°E/50°S (Figure 5a). In order to identify dominant modes of variability for each subregion, such anomalies were correlated with monthly anomalies of the climate indices by computing squared wavelet coherence spectra. Unreliable and less significant wavelet results can be produced if the probability density function (PDF) of geophysical time series is far from normally distributed [*Grinsted et al*., 2004]. Following *Grinsted et al*. [2004], this lack of normality can be addressed by transforming the time series of the anomalies of the wave parameters into time series of percentiles. Then, both the wave parameters and climate indices were normalized by their standard deviation in order to have total energy equal to one at all scales. Finally, the wavelet technique was applied. Power spectra were calculated using the Morlet function with nondimensional frequency equal to six for satisfying the admissibility condition [*Farge*, 1992]. Statistically significant signals were calculated using the chi-squared test for power spectra, since the wavelet power spectrum is chi-square distributed, and using 300 Monte Carlo simulations for coherence spectra. Significance at the 95% and 90% confidence levels were used for the power and coherence spectra, respectively. The cone-of-influence, where edge effects become important [*Torrence and Compo*, 1998], was computed for the purpose of dealing with errors at the beginning and end of the wavelet spectrum.

For a given time period, anomalies result from the combination of the signal in all frequencies, and for this reason, it is not trivial to account for the exact contribution of each atmospheric oscillation mode on the amplitudes of the anomalies of the wave parameters.

The squared wavelet coherence spectra of H_s with the climate indices are displayed in Figures 6–8. Hatched areas represent the cone-of-influence, and the 90% confidence levels are represented by thick contours. In phase and antiphase signals are represented by arrows pointing upward and downward, respectively, while arrows pointing rightward represent climate patterns preceding H_s, and the converse is true for arrows pointing leftward. The graphics related to the ZW3 index (Figure 7b) range from 1979 to 2001 due to lack of data in previous periods.

The H_s was most affected by IOD and ENSO cycles in the western cluster (Figure 6). Significant correlations with the DMI (Figure 6a) and SOI (Figure 6b) were observed in cycles with periodicities ranging from approximately 2 to 6 years from the early 1970s to late 1990s. In general, positive/negative phases of the IOD/ENSO were accompanied by large waves (positive anomalies of H_s) in the western cluster during this period, which is indicated by upward/downward arrows for the IOD/ENSO. This pattern can also be noted in the eastern and southern clusters, corroborating the correlation coefficient analysis. Examples of this relationship are described as follows. It is worth mentioning that the opposite convention in relation to *Saji et al*. [1999] has been used here for positive and negative phases of the ENSO, since they use Niño 3 SST anomalies (El Niño [+]; La Niña [−]) and we use the SOI (El Niño [−]; La Niña [+]). Concomitant positive IOD and negative ENSO extreme events occurred in 1972 [*Saji et al*., 1999] and 1997 [*Saji et al*., 1999; *Cai et al*.,

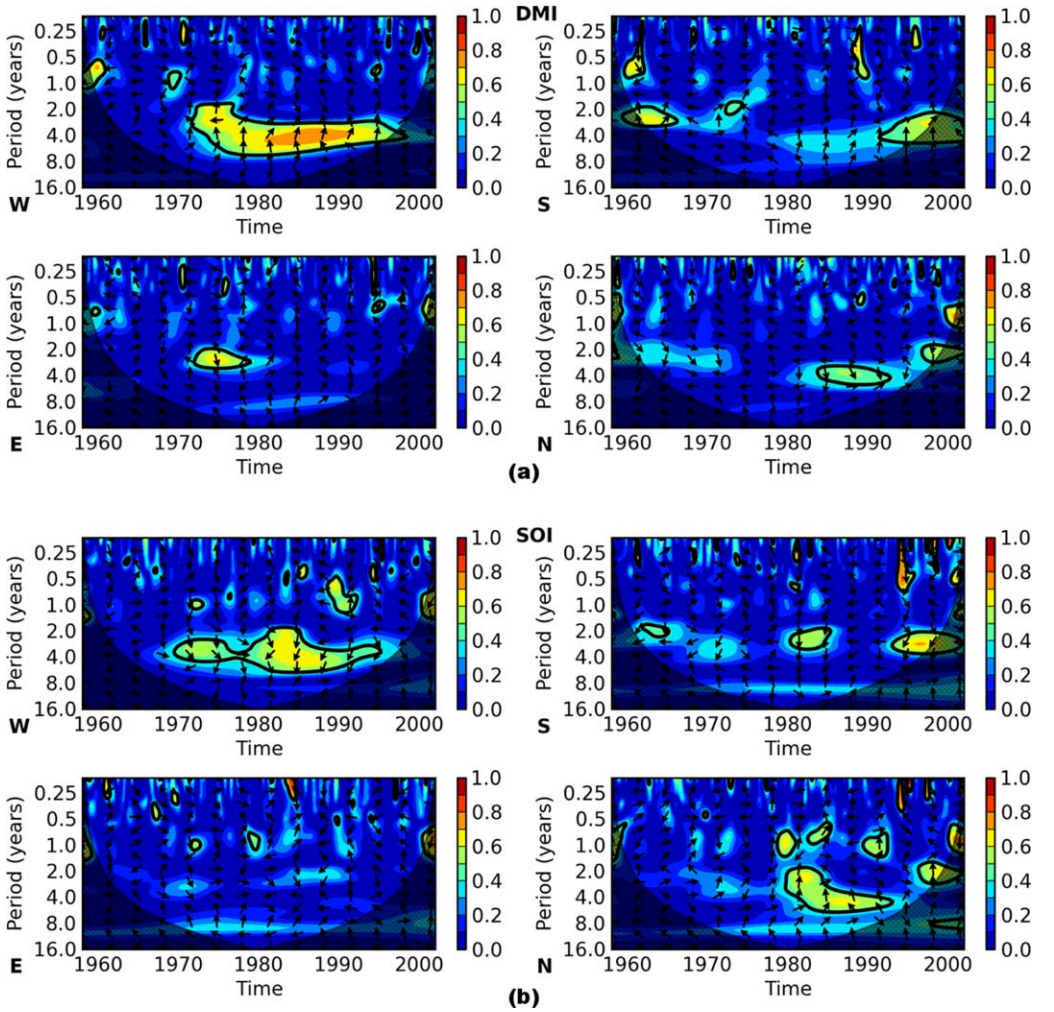

Figure 6. Squared wavelet coherence spectra of significant wave height with the: (a) DMI and (b) SOI. The 90% confidence levels are represented by thick contours, and hatched areas represent the cone-of-influence. In phase and antiphase signals are represented by arrows pointing upward and downward, respectively. Arrows pointing rightward represent climate patterns preceding H_s, whereas the converse is true for arrows pointing leftward. The letters W, S, E, and N in the lower left corner of the graphics stand for western, southern, eastern, and northern clusters, respectively.

2014]. In the first, the IOD was associated with H_s through ~3 year cycles in the western and eastern clusters, and 2 year cycles in the southern cluster (Figure 6a). Short-lived annual signals in the western and eastern clusters, and ~3 year cycles in the western cluster were found to be associated with the ENSO (Figure 6b). In the second concomitant extreme event (1997), H_s showed correlations with the DMI in the western and southern clusters at periodicities of approximately 4 years (Figure 6a), while ~3 year cycles related to the ENSO were highlighted in the southern cluster (Figure 6b). The moderate IOD event of 1982 [*Cai et al*., 2014] in combination with the extreme ENSO event in the same year [*Cai et al*., 2015] also led to large waves. Correlations with the DMI and SOI were observed in the western cluster with ~4 year cycles in addition to correlations with the SOI in the southern cluster at the ~3 year time scale. The extreme IOD event occurred in 1994 [*Cai et al*., 2014; *Saji et al*., 1999] presented strong correlations with H_s in the western and southern clusters during its positive phase at periodicities of approximately 4 years (Figure 6a). Strong correlations of H_s with the SOI, with cycles of approximately 4 years in the western cluster, and of 0.5 year and approximately 3 years in the southern cluster, were also noted in 1994 (Figure 6b), and might have been triggered by the IOD due to its relationship with the ENSO. Another extreme IOD event, reported by *Saji et al*. [1999], took place in 1961. This had an effect on H_s only in the southern cluster at periodicities of approximately 3 years (Figure 6a). As discussed in the correlation coefficient subsection, positive anomalies of H_s are generally seen during negative/positive phases of the IOD/ENSO in the northern cluster. Knowing

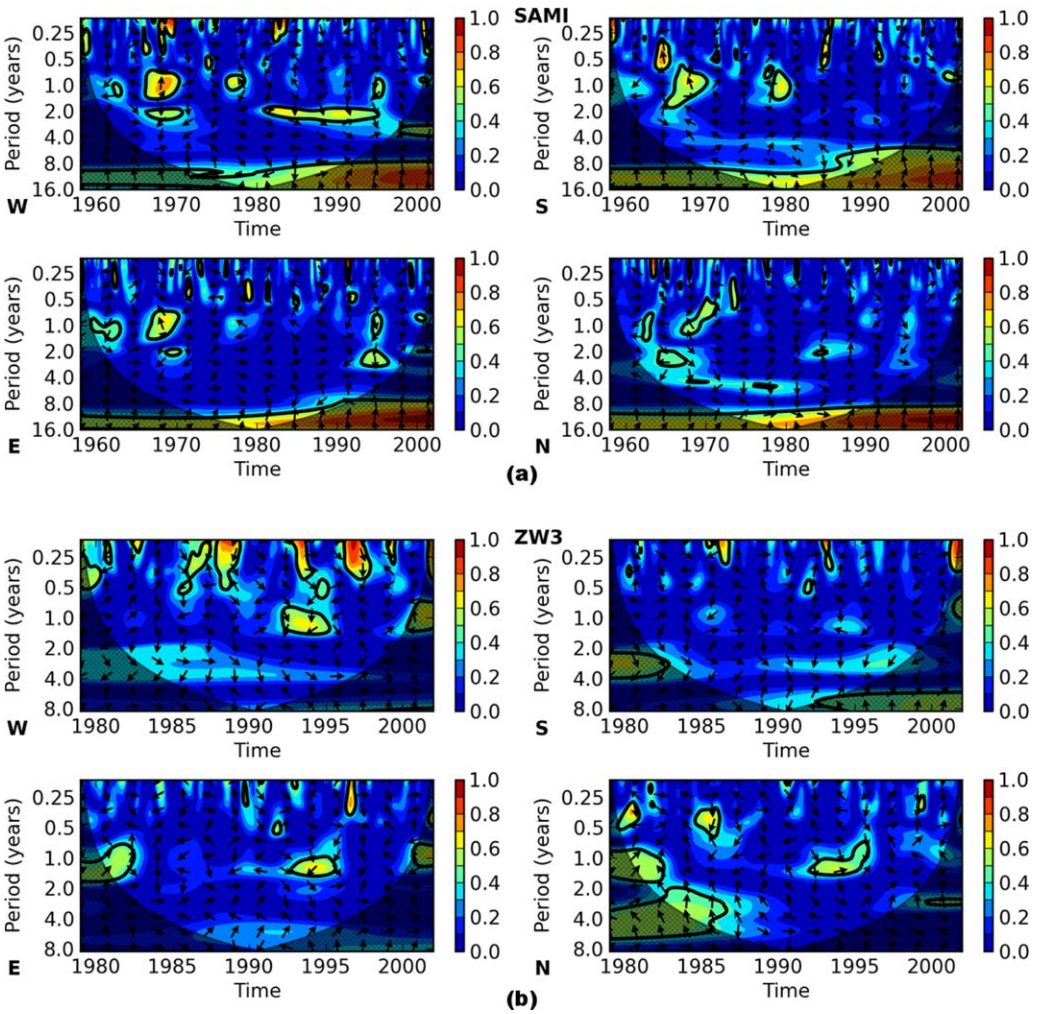

Figure 7. Squared wavelet coherence spectra of significant wave height with the: (a) SAMI and (b) ZW3 index. The 90% confidence levels are represented by thick contours, and hatched areas represent the cone-of-influence. In phase and antiphase signals are represented by arrows pointing upward and downward, respectively. Arrows pointing rightward represent climate patterns preceding H_s, whereas the converse is true for arrows pointing leftward. The letters W, S, E, and N in the lower left corner of the graphics stand for western, southern, eastern, and northern clusters, respectively.

that El Niño conditions prevailed during the extreme ENSO event of 1982, one observes decreases in H_s in the northern cluster in this year, indicated by upward arrows in all time scales with significant correlations (Figure 6b). Extreme La Niña events occurred in 1988–1989 and 1998–1999 [*Cai et al.*, 2015]. Their signatures can be clearly seen in the northern cluster at ~5 and ~2 year cycles, respectively (Figure 6b). In contrast, downward arrows suggest decreases in H_s in the southern cluster in 1998–1999. The IOD negative phase was rather weak and short during 1988–1989, and stronger and longer during 1998–1999. However, signals with cycles of approximately 4 and 2 years, respectively, were still apparent in both periods in the northern cluster, suggesting influence of the ENSO on the IOD.

Remarkable long-term (longer than 8 years) cycles are noted in the wavelet coherence spectra of H_s with the SAMI in all clusters (Figure 7a). Although these features are under influence of edge effects, which means they should be treated with caution, *Gong and Wang* [1999] reinforce the importance of examining the decadal variability of the SAM. Correlations of H_s with the SAMI in decadal time scales were strengthened from the late 1980s onward, and upward arrows indicate larger waves associated with positive phases of the SAM during this period. Regarding shorter time scales, the strongest correlations of H_s with the SAMI were found in the western cluster, with cycles generally shorter than approximately 4 years. The weakest correlations were seen in the northern cluster, with the strongest signals prevailing from seasonal to ~3 year cycles until the mid-1970s. The influence of the SAM on H_s in the southern and eastern clusters was

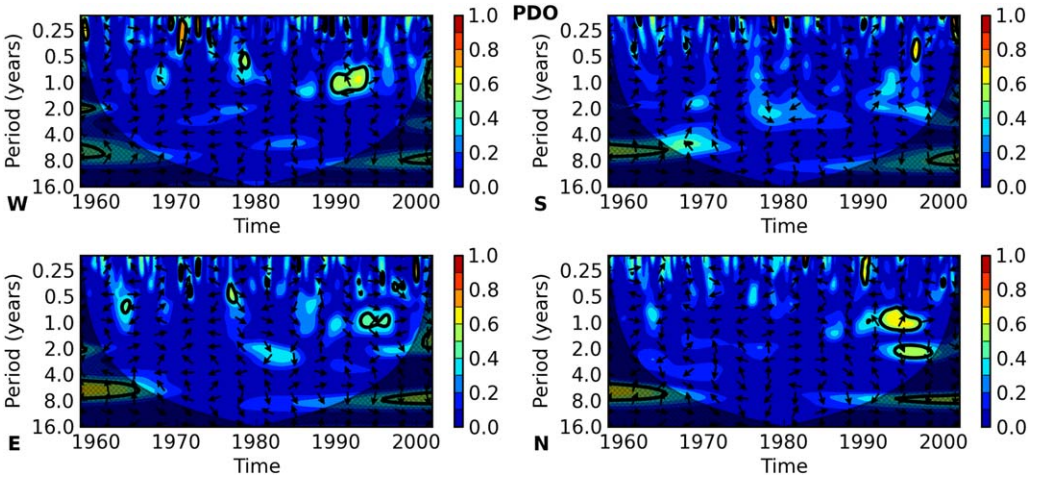

Figure 8. Squared wavelet coherence spectra of significant wave height with the PDO index. The 90% confidence levels are represented by thick contours, and hatched areas represent the cone-of-influence. In phase and antiphase signals are represented by arrows pointing upward and downward, respectively. Arrows pointing rightward represent climate patterns preceding H_s, whereas the converse is true for arrows pointing leftward. The letters W, S, E, and N in the lower left corner of the graphics stand for western, southern, eastern, and northern clusters, respectively.

moderate in comparison to the other two clusters. Seasonal to interannual cycles, with periodicities of up to approximately 2 years, were seen in the southern cluster mainly until the late 1970s, while slightly longer cycles of up to approximately 3 years could be noted in the eastern cluster. Strong correlations at annual time scale occurred in the late 1960s, and were highlighted in all clusters. They followed the onset of the trend toward the positive phase of the SAM, which has been occurring since the mid-1960s [*Marshall*, 2003]. Upward arrows indicate that positive SAM was accompanied by positive anomalies of H_s in the late 1960s. The SAMI and H_s also presented strong correlations at seasonal time scales in the western cluster in this period. In the same cluster, a ~2 year cycle was dominant from the early 1980s to mid-1990s, when large waves were associated with negative phases of the SAM. With respect to the ZW3, very distinct patterns were observed among the clusters (Figure 7b). According to *Raphael* [2004], significant fluctuations of the ZW3 resulted in rapid change from the atmospheric meridional flow to zonal flow in 1986–1987 and 1993–1995, which coincided with periods of strong correlations with H_s in the western cluster at seasonal and intraseasonal time scales. Another strongly correlated signal at the same time scales took place in 1996–1997, resulting in large waves when the atmospheric zonal flow was migrating to meridional flow [*Raphael*, 2004]. In the same cluster, signals of the annual cycle described by *Raphael* [2004] were apparent in the mid-1990s and early 2000s. The main cycle in the eastern cluster was also highlighted at the annual time scale. The southern and northern clusters presented correlations at interannual time scales, from approximately 2 to 8 years, but most of them were under influence of edge effects. Apart from those cycles, H_s in the southern cluster was little influenced by the ZW3, showing strong correlations only in short-lived signals at seasonal time scales. In the northern cluster, the annual cycle of the ZW3 was correlated with H_s in the early 1980s and mid-1990s, while the biannual cycle was more evident until the mid-1980s.

The PDO index and H_s were weakly correlated in all clusters (Figure 8). Despite being under influence of edge effects, statistically significant interannual PDO cycles, between 5 and 7 years, affected H_s until the mid-1960s and after the mid-1990s. Correlations at the annual time scale were also observed in the 1990s, except in the southern cluster, when large waves were associated with positive PDO. An additional 2 year cycle was accentuated in the northern cluster in the mid-1990s.

The squared wavelet coherence spectra of the climate indices with the other wave parameters (not shown) presented analogous structure to the squared wavelet coherence spectra of H_s with the climate indices. Obviously, some cycles were either stronger or weaker than the ones just mentioned, and were either longer or shorter. Some of the strong statistically nonsignificant signals seen in the coherence spectra of the climate indices with H_s showed statistically significance in the squared wavelet coherence spectra of climate indices with the other wave parameters. In addition to that, some features noted only in certain clusters occasionally became apparent in others. Therefore, only noteworthy differences are mentioned below.

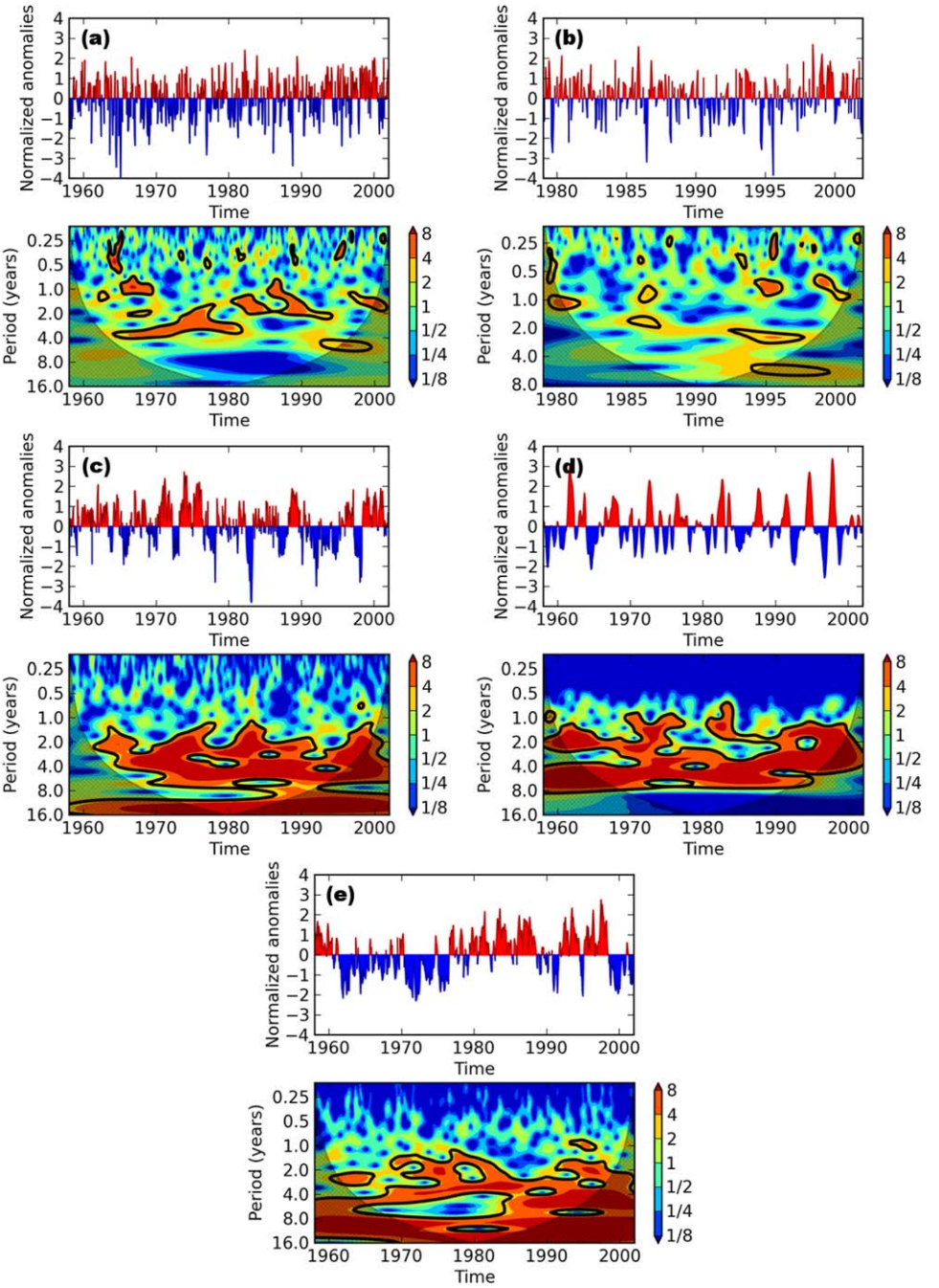

Figure 9. (top) Normalized anomalies of the climate indices with their corresponding (bottom) power spectra: (a) SAMI, (b) ZW3 index, (c) SOI, (d) DMI, and (e) PDO index. The 95% confidence levels are represented by thick contours, and hatched areas represent the cone-of-influence.

The greatest differences relative to H_s were generally found in the coherence spectra of D_p with the climate indices. In relation to the IOD, significant correlations with D_p at seasonal and intraseasonal time scales were more frequently identified in the southern and northern clusters. Larger extreme waves ($90thH_s$) were associated with positive IOD in the eastern cluster due to substantially strong correlations at ~3 year time scales in the 1970s. In the same cluster, large wave periods (T_{mean} and T_p) correlated with positive IOD at interannual time scales, from 1 to 4 years, from the late 1950s to mid-1970s and from the mid-1990s to early 2000s. Regarding the ENSO, strong correlations with D_p occurred in the eastern cluster at seasonal, intraseasonal, and annual time scales in the early 1970s. Additionally, a 8–14 year band extending during the whole hindcast period in the western cluster indicated counterclockwise/clockwise rotation of D_p in El Niño/La

Table 1. Correlation Coefficients Among the Climate Indices for the Period 1958–2001[a]

	SAMI	SOI	DMI	PDO Index
SOI	0.05			
DMI	**0.09**	**−0.29**		
PDO index	−0.01	**−0.35**	−0.04	
ZW3 index	**0.21**	0.06	−0.04	−0.08

[a]Correlations with the ZW3 index comprise the period 1979–2001. Statistically significance within 95% is represented by bold font.

Niña events. This band was replicated in the southern cluster for $90thH_s$, contributing with decreases in $90thH_s$ during El Niño years. Large T_{mean} was correlated with El Niño events at interannual cycles, from 1.5 to approximately 4 years, in the eastern cluster, which were highlighted from the late 1950s to early 1970s and from the early 1980s to early 2000s. With respect to the SAM, counterclockwise rotation of D_p accompanied its positive phase in the northern cluster at interannual time scales, from approximately 3 to 6 years. Wave periods (T_{mean} and T_p) were strongly influenced by the SAM in all clusters during the whole hindcast period. Considerably stronger correlations in comparison to the other wave parameters were found at seasonal, intraseasonal, annual, and interannual time scales. In general, larger wave periods were associated with positive SAM, except in the northern cluster, where the reverse pattern was occasionally observed. Strong correlations of the ZW3 with D_p were found in the southern cluster at time scales between approximately 0.5 and 2 years in the early 1980s and from the early 1990s to early 2000s. Larger wave periods (T_{mean} and T_p) correlated with the atmospheric meridional flow (positive ZW3) in the 4–8 year band in the 1990s, except in the northern cluster. Clockwise rotation of D_p and positive PDO phases were strongly correlated in the western cluster from the late 1950s to late 1980s, presenting cycles that ranged from seasonal to 8 years. Finally, larger wave periods (T_{mean} and T_p) were associated with positive PDO in the western and southern clusters in the 2–8 year band in the 1970s.

The anomalies of wave parameters are enhanced or reduced when climate modes coincide in time and frequency. The climate modes have overlapped in several periods of time, as can be noted in Figure 9, which shows normalized anomalies (top) of the climate indices with their corresponding power spectra (bottom). The anomalies provide information on the climate mode phases and how strong they were. On the other hand, they do not explain the exact percentage of variance related to each cycle. As this issue is beyond the scope of this work, the variance related to each cycle is not analyzed. Thus, for the purpose of understanding interrelationships of the climate patterns, correlation coefficients (R) were computed for the monthly mean anomaly time series of their indices during the hindcast period (Table 1). The largest correlation occurs between the SOI and PDO index ($R = -0.35$), which strongly covaried in the early 1970s and in the 1990s (Figures 9c and 9e). The negative nature of this correlation is in agreement with *Mantua et al.* [1997]. A correlation of $R = -0.29$ between the SOI and DMI reinforces the works by *Schott et al.* [2009] and *Izumo et al.* [2010], and is associated with cycles that covaried at interannual time scales between approximately 1.5 and 6 years (Figures 9c and 9d). *Yuan and Li* [2008] stated that the ZW3 is rather independent from the SAM. However, a statistically significant correlation of $R = 0.21$ was found despite the little variability shared by the modes (Figures 9a and 9b). The SAMI and DMI presented a low but statistically significant correlation of $R = 0.09$, which is related to cycles that covaried at time scales between 0.5 and 4 years (Figures 9a and 9d). *Raphael* [2004] suggested a possible relationship between the ZW3 and ENSO, but a statistically nonsignificant correlation of only $R = 0.06$ was obtained. The SOI and SAMI are positively correlated but not statistically significant, as previously reported by *Harley et al.* [2010]. However, *Stammerjohn et al.* [2008] showed that when positive/negative phases of both the ENSO and SAM occurred simultaneously, the high-latitude ice-atmosphere response to the ENSO was stronger than when they were not concurrent.

7. Conclusions

The influence of climate patterns on the wave climate around New Zealand and the surrounding southwest Pacific Ocean has been explored in detail in this study. The results of a 45 year (1957–2002) wave hindcast were compared to atmospheric oscillations over several time scales. First, the mean annual and interannual variabilities of H_s were computed with the purpose of verifying sites susceptible to large variations in relation to average wave conditions. Then, the PDO, ENSO, IOD, SAM, and ZW3 modes were correlated with five simulated wave parameters. The interactions of D_p, T_p, T_{mean}, H_s, and $90thH_s$ with the climate modes were assessed by correlation coefficients and squared wavelet coherence spectra.

In general, relatively low correlation coefficients of climate patterns with wave parameters were obtained, with the maximum value reaching 0.45. The relatively weak correlations show that many factors contribute to the variability of the wave climate in the region of study. Positive correlations of the wave parameters with the SAMI in the highest latitudes of the regional domain arise from the strengthening of westerly winds generated by stronger pressure gradient between 40°S and 65°S during its positive phase. The SAM is the most important climate pattern for wave direction, which rotates clockwise south of the country and counterclockwise along and off the west and north coasts during positive SAM phases. The zonal wind stress anomaly induces larger waves in New Zealand during negative phases of the ZW3. The ENSO also plays a significant role, with northeasterly winds producing larger waves to the north of New Zealand during La Niña phases, while southwesterly winds cause larger waves around the rest of the country in El Niño events. Positive phases of the PDO contribute to increasing wave height and wave period mainly in the west and south coasts. The influence of the IOD on the wave climate is also more significant during its positive phases, when wave periods are mostly affected off the east and west coasts, and wave heights are primarily impacted off the south coast. Correlations of H_s with the SOI using seasonally averaged results were also conducted (not shown) and presented substantially higher statistically significant values than monthly averaged results. An example that reinforces such stronger correlations is the warming in the tropical Indian Ocean due to the ENSO takes approximately 3–6 months to occur [*Deser et al*., 2010]. According to *Harley et al*. [2010], seasonally averaged SOI values are more suitable for correlations with other parameters than monthly averaged values, since the latter produce a noncoherent pattern due to the inherent noisiness of its time series at short time scales. This issue is beyond the scope of the present work, but deserves further investigation in future studies.

The correlation coefficient analysis provided a good overview of the spatial distribution of the relationship between the wave parameters and different phases of the climate modes. However, information on how this distribution has evolved in time cannot be extracted from such analysis. Thus, this was accomplished by using wavelet coherence spectra. A cluster analysis was used to divide the regional domain into distinct wave climates, which enabled the assessment of the dominant modes of variability related to each climate pattern through the use of spectral analysis. The latter revealed that the wave parameters exhibited remarkable cycles throughout the hindcast period. Strong correlations at interannual time scales were identified during extreme events of the ENSO and IOD modes. Decadal variability of the SAM showed substantial relationship with the wave parameters, especially from the late 1980s to early 2000s. A number of authors [e.g., *Young et al*., 2011, 2012; *Wentz et al*., 2007] have found increasing trends in wave height and wind speed. Whether these trends are related to either long-term trends or atmospheric oscillations varying at decadal time scales is an issue that remains open. Our results support the relationship between increases in wave height and the intensification of the SAM in recent decades. Nevertheless, decadal time scales are in a region of the spectrum that does not allow us to make conclusive inferences. A longer-duration data set is needed to further investigate this question. The SAM also affected the wave parameters at seasonal, annual, and interannual time scales, principally in the western cluster, which in turn was the most impacted by all climate patterns tested. During significant fluctuations of the ZW3, when the atmospheric flow rapidly changed from meridional to zonal and vice versa, strong correlations with the wave parameters were highlighted at seasonal and intraseasonal time scales. The PDO presented the weakest correlation with wave parameters, influencing more the peak wave direction with clockwise rotation during its positive phase.

The MAV and IAV results revealed high variability in coastal areas, especially in sheltered regions where little or no significant trend in H_s was identified. In general, an increasing trend in H_s was observed around the country, with values varying between 1 and 6 cm/decade near the shoreline. Correlation coefficients confirmed that coastal areas are generally more affected by the climate modes than offshore regions, and consequently are more vulnerable to climate changes. These results suggest, for instance, that habitats such as the mangrove forests, which extend down to approximately 38°S in New Zealand, might experience greater stress during certain phases of atmospheric oscillations, since successful seedling establishment is sensitive to wave energy [*Balke et al*., 2013]. However, as shown by *Lovelock et al*. [2010], atmospheric oscillations can also favor mangrove forests expansion. Changes in the wave climate might impact in the physiological structure and survivorship of marine organisms. Kelps, for example, differ in morphology according to their wave exposure [*Nanba et al*., 2011], and relationships between storm waves during ENSO events and mortality of kelp forests have been documented by *Dayton et al*. [1992]. In New Zealand, *Schiel and Thompson* [2012] suggested that the growth rate of kelp is associated with wave height and wave direction.

In terms of coastal engineering, beach erosion, which increasingly has been shown to vary around the Pacific [*Barnard et al*., 2015] and in New Zealand with wave climate variations [e.g., *de Lange*, 2001], represents a major problem for the expanding coastal population of the country. Our results also provide further support to the existence of climate-cycle driven temporal patterns in sand spit erosion and accretion, which have occurred in opposing phases between the east and west coasts of the upper north island of New Zealand [*Bryan et al*., 2008]. The opposing cycles of erosion and accretion between the Ohiwa spit and Mokau spit in *Bryan et al*. [2008], which are located in the northern and western clusters (locations given in Figure 1), respectively, were hypothesized to be caused by the shift to positive PDO in the early 1980s. Our results suggest that opposing changes to wave heights in the western and northern clusters could more likely be driven by changes to the IOD and ENSO, since both showed a strengthening of the signal in these sectors during this time period (Figures 6a and 6b). The SOI also becomes more negative during this time (Figure 9c), which is correlated with an increase in wave height on the west coast and decrease on the northeast coast. The increase in the correlation of H_s with the DMI in the west coast (Figure 6a), which occurred at the 4 year cycle at the beginning of the 1980s, might also have contributed to the observed increased erosion. Erosion processes are known to be nonlinear, with recovery time scale much longer than the accretion time scale [*Yates et al*., 2009], and so a period of severe erosion may not be balanced by a period of severe accretion in the same way as a period of minor erosion is compensated by a period of mild accretion. Therefore, a more variable wave condition could explain the increase in beach erosion. The PDO is not a strong driver of wave height on the northeast coast, but the correlation is generally opposite between the northern and western clusters. Spits also accrete by alongshore transport (driven by wave angle changes) in addition to cross-shore transport (driven by wave height changes), and so the northeast coast accretion during the 1980s could be associated with the shift to wave directions more toward the north that occur during the positive phases of the PDO in the northern cluster (Figure 4).

This work showed the importance of including multiple climate modes in order to completely understand the drivers of wave parameter changes, since the modes superimpose and occasionally trigger each other. We recommend that more work be undertaken on interactions between two or more atmospheric oscillation modes in periods of time that modes share strong anomalies. Nevertheless, these results clearly show how the dominant drivers vary around the diverse coastline of New Zealand, and, as suggested by previous authors, can provide a proxy with which to improve our ability to predict the impacts of future climate change on the wave climate.

Appendix A: Acronyms and Their Respective Meanings

This appendix provides a summary of the acronyms used throughout the main text along with their respective meanings (Table A1).

Table A1. Acronyms and Their Respective Meanings

Atmospheric Oscillations and Their Respective Indices			
AAO	Antarctic Oscillation	AOI	Antarctic Oscillation Index
IOD	Indian Ocean Dipole	DMI	Dipole Mode Index
ENSO	El Niño-Southern Oscillation	SOI	Southern Oscillation Index
SAM	Southern Annular Mode	SAMI	Southern Annular Mode Index
ZW3	Zonal Wave-number-3 Pattern		
PDO	Pacific Decadal Oscillation		
Oceanographic and Atmospheric Variables			
D_p	Peak wave direction	SLP	Sea level pressure
H_s	Significant wave height	$90thH_s$	Ninetieth percentile significant wave height
T_p	Peak wave period	T_{mean}	Mean wave period
SST	Sea surface temperature		
Statistical Parameters and Numerical Approximations			
DIA	Discrete interaction approximation	PDF	Probability density function
MAV	Mean annual variability	IAV	Interannual variability
R	Pearson's correlation coefficient	RMSE	Root-mean-square error
Institution and Project Names			
BAS	British Antarctic Survey	NGDC	National Geophysical Data Center
JAMSTEC	Japan Agency for Marine-Earth Science and Technology	JMA	Japan Meteorological Agency
JONSWAP	Joint North Sea Wave Project	NDBC	National Data Buoy Center
ECMWF	European Centre for Medium-Range Weather Forecasts	NOAA	National Oceanic and Atmospheric Administration

Acknowledgments:
The SOI, DMI, SAMI, PDO index, and ZW3 index data are available at the websites of the National Oceanic and Atmospheric Administration (http://www.cpc.ncep.noaa.gov/data/indices/soi), Japan Agency for Marine-Earth Science and Technology (http://www.jamstec.go.jp/frcgc/research/d1/iod/DATA/dmi_HadISST.txt), British Antarctic Survey (http://www.nerc-bas.ac.uk/icd/gjma/sam.html), Japan Meteorological Agency (http://www.data.jma.go.jp/gmd/kaiyou/data/db/climate/pdo/pdo.txt), and *Raphael* [2004], respectively. The ERA-40 and ETOPO1 data are available at http://apps.ecmwf.int/datasets/data/era40-daily/and http://www.ngdc.noaa.gov/mgg/global/, respectively. The buoy and satellite data used for validation of the 45 year wave hindcast are available at http://www.ndbc.noaa.gov/and http://globwave.ifremer.fr/. Finally, all other data used to produce the results published in this article are available upon request made to the first and third authors, victorgodoirj@gmail.com and richard.gorman@niwa.co.nz, respectively. This research has been funded by the Coordenação de Aperfeiçoamento de Pessoal de Nível Superior (CAPES), grant BEX9551/13-1. The 45 year wave hindcast was conducted under the scope of the "Wave and storm-surge projections" (WASP) project, funded through the New Zealand Ministry of Science and Innovation, contract C01X0806. The authors are thankful to Marilyn *Raphael* for providing the ZW3 index data, and to the other data sources mentioned throughout the text, NOAA, ECMWF, JAMSTEC, BAS, and JMA. Finally, we would like to thank Alex Port for his valuable comments on the techniques used in this work, Felipe Marques for his feedback regarding the spectral analysis, the two reviewers for insightful comments, and the Python community for knowledge sharing on programming language.

References

Alexander, M. A., I. Bladé, M. Newman, J. R. Lanzante, N. Lau, and J. D. Scott (2002), The Atmospheric Bridge: The influence of ENSO teleconnections on air-sea interaction over the global oceans, *J. Clim.*, *15*(16), 2205–2231, doi:10.1175/1520-0442(2002)015<2205:TABTIO>2.0.CO;2.

Amante, C., and B. W. Eakins (2009), ETOPO1 1 Arc-Minute Global Relief Model: Procedures, data sources and analysis, *NOAA Tech. Memo. NESDIS NGDC-24*, Natl. Geophys. Data Cent., NOAA, Boulder, Colo., doi:10.7289/V5C8276M.

Balke, T., T. J. Bouma, P. M. J. Herman, E. M. Horstman, C. Sudtongkong, and E. L. Webb (2013), Cross-shore gradients of physical disturbance in mangroves: Implications for seedling establishment, *Biogeosciences*, *10*, 5411–5419, doi:10.5194/bg-10-5411-2013.

Barnard, P. L., et al. (2015), Coastal vulnerability across the Pacific dominated by El Niño/Southern Oscillation, *Nat. Geosci.*, *8*, 801–807, doi:10.1038/ngeo2539.

Bell, R. G., D. G. Goring, and W. P. de Lange (2000), Sea-level change and storm surges in the context of climate change, *Inst. Prof. Eng. N. Z. Trans.*, *27*(1), 1–10.

Bosserelle, C., P. Charitha, and I. Haigh (2012), Inter-annual variability and longer-term changes in the wave climate of Western Australia between 1970 and 2009, *Ocean Dyn.*, *62*(1), 63–76, doi:10.1007/s10236-011-0487-3.

Bryan, K. R., P. S. Kench, and D. E. Hart (2008), Multi-decadal coastal change in New Zealand: Evidence, mechanisms and implications, *N. Z. Geogr.*, *64*(2), 117–128, doi:10.1111/j.1745-7939.2008.00135.x.

Cai, W., P. G. Baines, and H. B. Gordon (1999), Southern mid- to high-latitude variability, a Zonal Wavenumber-3 Pattern, and the Antarctic circumpolar wave in the CSIRO coupled model, *J. Clim.*, *12*(10), 3087–3104, doi:10.1175/1520-0442(1999)012<3087:SMTHLV>2.0.CO;2.

Cai, W., A. Santoso, G. Wang, E. Weller, L. Wu, K. Ashok, Y. Masumoto, and T. Yamagata (2014), Increased frequency of extreme Indian Ocean Dipole events due to greenhouse warming, *Nature*, *510*, 254–258, doi:10.1038/nature13327.

Cai, W., et al. (2015), Increased frequency of extreme La Niña events under greenhouse warming, *Nat. Clim. Change*, *5*, 132–137, doi:10.1038/nclimate2492.

Caires, S., V. R. Swail, and X. L. Wang (2006), Projection and analysis of extreme wave climate, *J. Clim.*, *19*(21), 5581–5605, doi:10.1175/JCLI3918.1.

Cane, M. A. (2005), The evolution of El Niño, past and future, *Earth Planet. Sci. Lett.*, *230*(3), 227–240, doi:10.1016/j.epsl.2004.12.003.

Cavaleri, L., and P. Malanotte-Rizzoli (1981), Wind-wave prediction in shallow water: Theory and applications, *J. Geophys. Res.*, *86*(C11), 10,961–10,973, doi:10.1029/JC086iC11p10961.

Chiswell, S. M., H. C. Bostock, P. J. H. Sutton, and M. J. M. Williams (2015), Physical oceanography of the deep seas around New Zealand: A review, N. Z. *J. Mar. Freshwater Res.*, *49*(2), 286–317, doi:10.1080/00288330.2014.992918.

Coggins, J. H. J., S. Parsons, and D. Schiel (2015), An assessment of the ocean wave climate of New Zealand as represented in Kidson's synoptic types, *Int. J. Climatol.*, *36*, 2481–2496, doi:10.1002/joc.4507.

Cox, A. T., and V. R. Swail (2001), A global wave hindcast over the period 1958-1997: Validation and climate assessment, *J. Geophys. Res.*, *106*(C2), 2313–2329, doi:10.1029/2001JC000301.

Davis, R. E. (2005), Intermediate-depth circulation of the Indian and South Pacific oceans measured by autonomous floats, *J. Phys. Oceanogr.*, *35*(5), 683–707, doi:10.1175/JPO2702.1.

Dayton, P. K., M. J. Tegner, P. E. Parnell, and P. B. Edwards (1992), Temporal and spatial patterns of disturbance and recovery in a kelp forest community, *Ecol. Monogr.*, *62*(3), 421–445, doi:10.2307/2937118.

de Lange, W. P. (2001), Interdecadal Pacific Oscillation (IPO): A mechanism for forcing decadal scale coastal change on the northeast coast of New Zealand?, *J. Coastal Res.*, *34*, 657–664.

Deser, C., M. A. Alexander, S. Xie, and A. S. Phillips (2010), Sea surface temperature variability: Patterns and mechanisms, *Annu. Rev. Mar. Sci.*, *2*, 115–143, doi:10.1146/annurev-marine-120408-151453.

Farge, M. (1992), Wavelet transforms and their applications to turbulence, *Annu. Rev. Fluid Mech.*, *24*, 395–457, doi:10.1146/annurev.fl.24.010192.002143.

Garreaud, R., and D. S. Battisti (1999), Interannual (ENSO) and Interdecadal (ENSO-like) variability in the Southern Hemisphere tropospheric circulation, *J. Clim.*, *12*(7), 2113–2123, doi:10.1175/1520-0442(1999)012<2113:IEAIEL>2.0.CO;2.

Gillett, N. P., and D. W. J. Thompson (2003), Simulation of recent Southern Hemisphere climate change, *Science*, *302*(5643), 273–275, doi:10.1126/science.1087440.

Godoi, V. A., K. R. Bryan, and R. M. Gorman (2015), Spectral Analysis of the influence of the El Niño-Southern Oscillation on the north and south wave climates of New Zealand, Australasian Coasts & Ports Conference 2015, in *22nd Australasian Coastal and Ocean Engineering Conference and the 15th Australasian Port and Harbour Conference*, pp. 320-324, Eng. Aust., Auckland, New Zealand.

Gong, D., and S. Wang (1999), Definition of Antarctic Oscillation index, *Geophys. Res. Lett.*, *26*(4), 459–462, doi:10.1029/1999GL900003.

Gordon, N. D. (1986), The Southern Oscillation and New Zealand weather, *Mon. Weather Rev.*, *14*, 371–387, doi:10.1175/1520-0493(1986)114<0371:TSOANZ>2.0.CO;2.

Goring, D. G., and R. G. Bell (1999), El Niño and decadal effects on sea-level variability in northern New Zealand: A wavelet analysis, N. Z. *J. Mar. Freshwater Res.*, *33*(4), 587–598, doi:10.1080/00288330.1999.9516902.

Gorman, R. M., K. R. Bryan, and A. K. Laing (2003a), Wave hindcast for the New Zealand region: Nearshore validation and coastal wave climate, N. Z. *J. Mar. Freshwater Res.*, *37*(3), 567–588, doi:10.1080/00288330.2003.9517190.

Gorman, R. M., K. R. Bryan, and A. K. Laing (2003b), Wave hindcast for the New Zealand region: Deep-water wave climate, N. Z. *J. Mar. Freshwater Res.*, *37*(3), 589–612, doi:10.1080/00288330.2003.9517191.

Gorman, R. M., R. G. Bell, E. M. Lane, P. A. Gillibrand, and S. A. Stephens (2010), New Zealand wave climate—Simulating the past and future, paper presented at New Zealand Coastal Society Annual Conference, New Zealand Coastal Society, Whitianga, New Zealand, 17-19 Nov.

Grinsted, A., J. C. Moore, and S. Jevrejeva (2004), Application of the cross wavelet transform and wavelet coherence to geophysical time series, *Nonlinear Processes Geophys.*, *11*, 561–566, doi:10.5194/npg-11-561-2004.

Harley, M. D., I. L. Turner, A. D. Short, and R. Ranasinghe (2010), Interannual variability and controls of the Sydney wave climate, *Int. J. Climatol.*, *30*(9), 1322–1335, doi:10.1002/joc.1962.

Hartigan, J. A., and M. A. Wong (1979), Algorithm AS 136: A K-Means clustering algorithm, *J. R. Stat. Soc., Ser. C*, *28*(1), 100–108, doi:10.2307/2346830.

Hasselmann, K., et al. (1973), Measurements of wind-wave growth and swell decay during the Joint North Sea Wave Project (JONSWAP), *Dtsch. Hydrogr. Z.*, *8*(12), Suppl. A, 95.

Hasselmann, S., K. Hasselman, J. H. Allender, and T. P. Barnett (1985), Computations and parameterizations of the nonlinear energy transfer in a gravity-wave spectrum, Part II: Parameterizations of the nonlinear energy transfer for application in wave models, *J. Phys. Oceanogr.*, *15*(11), 1378–1391, doi:10.1175/1520-0485(1985)015<1378:CAPOTN>2.0.CO;2.

Hemer, M. A. (2010), Historical trends in Southern Ocean storminess: Long-term variability of extreme wave heights at Cape Sorell, Tasmania, *Geophys. Res. Lett.*, *37*, L18601, doi:10.1029/2010GL044595.
Hemer, M. A., J. A. Church, and J. R. Hunter (2010), Variability and trends in the directional wave climate of the Southern Hemisphere, *Int. J. Climatol.*, *30*(4), 475–491, doi:10.1002/joc.1900.
Izaguirre, C., F. J. Méndez, M. Menéndez, and I. J. Losada (2011), Global extreme wave height variability based on satellite data, *Geophys. Res. Lett.*, *38*, L10607, doi:10.1029/2011GL047302.
Izumo, T., J. Vialard, M. Lengaigne, C. B. Montegut, S. K. Behera, J. Luo, S. Cravatte, S. Masson, and T. Yamagata (2010), Influence of the state of the Indian Ocean Dipole on the following year's El Niño, *Nat. Geosci.*, *3*, 168–172, doi:10.1038/ngeo760.
Kanungo, T., D. M. Mount, N. S. Netanyahu, C. D. Piatko, R. Silverman, and A. Y. Wu (2002), An efficient K-Means clustering algorithm: Analysis and implementation, *IEEE Trans. Pattern Anal. Mach. Intell.*, *24*(7), 881–892, doi:10.1109/TPAMI.2002.1017616.
Karoly, D. J. (1989), Southern Hemisphere circulation features associated with El Niño-Southern Oscillation events, *J. Clim.*, *2*(11), 1239–1252, doi:10.1175/1520-0442(1989)002<1239:SHCFAW>2.0.CO;2.
Kidson, J. W. (1988), Interannual variations in the Southern Hemisphere circulation, *J. Clim.*, *1*(12), 1177–1198, doi:10.1175/1520-0442(1988)001<1177:IVITSH>2.0.CO;2.
Kushner, P. J., I. M. Held, and T. L. Delworth (2001), Southern Hemisphere atmospheric circulation response to global warming, *J. Clim.*, *14*(10), 2238–2249, doi:10.1175/1520-0442(2001)014<0001:SHACRT>2.0.CO;2.
Laing, A. K. (1993), Estimates of wave height data for New Zealand waters by numerical modelling, N. Z. *J. Mar. Freshwater Res.*, *27*(2), 157–175, doi:10.1080/00288330.1993.9516554.
Laing, A. K. (2000), New Zealand wave climate from satellite observations, N. Z. *J. Mar. Freshwater Res.*, *34*(4), 727–744, doi:10.1080/00288330.2000.9516973.
Lavergne, C., J. B. Palter, E. D. Galbraith, R. Bernardello, and I. Marinov (2014), Cessation of deep convection in the open Southern Ocean under anthropogenic climate change, *Nat. Clim. Change*, *4*, 278–282, doi:10.1038/nclimate2132.
Likas, A., N. Vlassis, and J. J. Verbeek (2003), The global K-Means clustering algorithm, *Pattern Recognition*, *36*(2), 451–461, doi:10.1016/S0031-3203(02)00060-2.
Limpasuvan, V., and D. L. Hartmann (1999), Eddies and the annular modes of climate variability, *Geophys. Res. Lett.*, *26*(20), 3133–3136, doi:10.1029/1999GL010478.
Lovelock, C. E., B. K. Sorrell, N. Hancock, Q. Hua, and A. Swales (2010), Mangrove forest and soil development on a rapidly accreting shore in New Zealand, *Ecosystems*, *13*(3), 437–451, doi:10.1007/s10021-010-9329-2.
Mantua, N. J., and S. R. Hare (2002), The Pacific decadal oscillation, *J. Oceanogr.*, *58*(1), 35–44, doi:10.1023/A:1015820616384.
Mantua, N. J., S. R. Hare, Y. Zhang, J. M. Wallace, and R. C. Francis (1997), A Pacific interdecadal climate oscillation with impacts on salmon production, *Bull. Am. Meteorol. Soc.*, *78*(6), 1069–1079, doi:10.1175/1520-0477(1997)078<1069:APICOW>2.0.CO;2.
Marshall, G. J. (2003), Trends in the Southern Annular Mode from observations and reanalyses, *J. Clim.*, *16*(24), 4134–4143, doi:10.1175/1520-0442(2003)016<4134:TITSAM>2.0.CO;2.
Mo, K. C., and G. H. White (1985), Teleconnections in the Southern Hemisphere, *Mon. Weather Rev.*, *113*(1), 22–37, doi:10.1175/1520-0493(1985)113<0022:TITSH>2.0.CO;2.
Morris, M., B. Stanton, and H. Neil (2001), Subantarctic oceanography around New Zealand: Preliminary results from an ongoing survey, N. Z. *J. Mar. Freshwater Res.*, *35*(3), 499–519, doi:10.1080/00288330.2001.9517018.
Nanba, N., T. Fujiwara, K. Kuwano, Y. Ishikawa, H. Ogawa, and R. Kado (2011), Effect of water flow velocity on growth and morphology of cultured Undaria pinnatifida sporophytes (Laminariales, Phaeophyceae) in Okirai Bay on the Sanriku coast, Northeast Japan, *J. Appl. Phycol.*, *23*(6), 1023–1030, doi:10.1007/s10811-010-9635-2.
Pickrill, R. A., and J. S. Mitchell (1979), Ocean wave characteristics around New Zealand, N. Z. *J. Mar. Freshwater Res.*, *13*(4), 501–520, doi:10.1080/00288330.1979.9515827.
Quan, S., R. G. Kvitek, D. P. Smith, and G. B. Griggs (2013), Using vessel-based LIDAR to quantify coastal erosion during El Niño and Inter-El Niño periods in Monterey Bay, California, *J. Coastal Res.*, *29*(3), 555–565, doi:10.2112/JCOASTRES-D-12-00005.1.
Raphael, M. N. (2004), A zonal wave 3 index for the Southern Hemisphere, *Geophys. Res. Lett.*, *31*, L23212, doi:10.1029/2004GL020365.
Revell, C. G., and S. W. Goulter (1986), South Pacific tropical cyclones and the Southern Oscillation, *Mon. Weather Rev.*, *114*(6), 1138–1145, doi:10.1175/1520-0493(1986)114<1138:SPTCAT>2.0.CO;2.
Ropelewski, C. F., and P. D. Jones (1987), An extension of the Tahiti-Darwin Southern Oscillation Index, *Mon. Weather Rev.*, *115*(9), 2161–2165, doi:10.1175/1520-0493(1987)115<2161:AEOTTS>2.0.CO;2.
Russell, J. L., K. W. Dixon, A. Gnanadesikan, R. J. Stouffer, and J. R. Toggweiler (2006), The Southern Hemisphere westerlies in a warming world: Propping open the door to the deep ocean, *J. Clim.*, *19*, 6382–6390, doi:10.1175/JCLI3984.1.
Rusu, E., and C. Guedes Soares (2009), Numerical modelling to estimate the spatial distribution of the wave energy in the Portuguese nearshore, *Renewable Energy*, *34*(6), 1501–1516, doi:10.1016/j.renene.2008.10.027.
Saji, N. H., B. N. Goswami, P. N. Vinayachandran, and T. Yamagata (1999), A dipole mode in the tropical Indian Ocean, *Nature*, *401*, 360–363, doi:10.1038/43854.
Sallée, J.-B., R. J. Matear, S. R. Rintoul, and A. Lenton (2012), Localized subduction of anthropogenic carbon dioxide in the Southern Hemisphere oceans, *Nat. Geosci.*, *5*, 579–584, doi:10.1038/ngeo1523.
Sasaki, Y. N., S. Minobe, N. Schneider, T. Kagimoto, M. Nonaka, and H. Sasaki (2008), Decadal sea level variability in the South Pacific in a global eddy-resolving ocean model hindcast, *J. Phys. Oceanogr.*, *38*(8), 1731–1747, doi:10.1175/2007JPO3915.1.
Schiel, D. R., and G. A. Thompson (2012), Demography and population biology of the invasive kelp Undaria pinnatifida on shallow reefs in southern New Zealand, *J. Exp. Mar. Biol. Ecol.*, *434-435*, 25–33, doi:10.1016/j.jembe.2012.07.023.
Schott, F. A., S. Xie, and J. P. McCreary (2009), Indian Ocean circulation and climate variability, *Rev. Geophys.*, *47*, RG1002, doi:10.1029/2007RG000245.
Simmonds, I., and K. Keay (2000), Variability of Southern Hemisphere extratropical cyclone behavior, 1958-97, *J. Clim.*, *13*(2), 550–561, doi:10.1175/1520-0442(2000)013<0550:VOSHEC>2.0.CO;2.
Sinclair, M. R., J. A. Renwick, and J. W. Kidson (1997), Low-frequency variability of Southern Hemisphere sea level pressure and weather system activity, *Mon. Weather Rev.*, *125*, 2531–2543, doi:10.1175/1520-0493(1997)125%3C2531:LFVOSH%3E2.0.CO;2.
Stammerjohn, S. E., D. G. Martinson, R. C. Smith, X. Yuan, and D. Rind (2008), Trends in Antarctic annual sea ice retreat and advance and their relation to El Niño-Southern Oscillation and Southern Annular Mode variability, *J. Geophys. Res.*, *113*, C03S90, doi:10.1029/2007JC004269.
Stephens, S. A., and R. M. Gorman (2006), Extreme wave predictions around New Zealand from hindcast data, N. Z. *J. Mar. Freshwater Res.*, *40*(3), 399–411, doi:10.1080/00288330.2006.9517431.

Sterl, A., and S. Caires (2005), Climatology, variability and extrema of ocean waves: The web-based KNMI/ERA-40 wave atlas, *Int. J. Climatol.*, *25*(7), 963–977, doi:10.1002/joc.1175.

Stopa, J. E., K. F. Cheung, H. L. Tolman, and A. Chawla (2013), Patterns and cycles in the Climate Forecast System Reanalysis wind and wave data, *Ocean Modell.*, *70*, 207–220, doi:10.1016/j.ocemod.2012.10.005.

Storlazzi, C. D., J. B. Shope, L. H. Erikson, C. A. Hegermiller, and P. L. Barnard (2015), Future wave and wind projections for United States and United States-affiliated Pacific Islands, *U.S. Geol. Surv. Open File Rep.*, *2015-1001*, 1–426, doi:10.3133/ofr20151001.

Taylor, P. H., V. E. Barker, D. Bishop, and R. Eatock Taylor (2009), 100-year waves, teleconnections and wave climate variability, paper presented at 11th International Workshop on Wave Hindcasting and Forecasting, Environ. Canada, Halifax, Nova Scotia, Canada.

Tolman, H. L. (2009), User manual and system documentation of WAVEWATCH III version 3.14, *NOAA/NWS/NCEP/MMAB Tech. Note 276*, 194 pp + Appendices, NOAA, Camp Springs, Md. [Available at http://polar.ncep.noaa.gov/waves/wavewatch/wavewatch.shtml.]

Tolman, H. L., and D. V. Chalikov (1996), Source terms in a third-generation wind-wave model, *J. Phys. Oceanogr.*, *26*(11), 2497–2518, doi:10.1175/1520-0485(1996)026<2497:STIATG>2.0.CO;2.

Torrence, C., and G. P. Compo (1998), A practical guide to wavelet analysis, *Bull. Am. Meteorol. Soc.*, *79*(1), 61–78, doi:10.1175/1520-0477(1998)079<0061:APGTWA>2.0.CO;2.

Trenberth, K. E. (1980), Planetary waves at 500 mb in the Southern Hemisphere, *Mon. Weather Rev.*, *108*(9), 1378–1389, doi:10.1175/1520-0493(1980)108<1378:PWAMIT>2.0.CO;2.

Trenberth, K. E., and J. W. Hurrell (1994), Decadal atmosphere-ocean variations in the Pacific, *Clim. Dyn.*, *9*(6), 303–319, doi:10.1007/BF00204745.

Uppala, S. M., et al. (2005), The ERA-40 re-analysis, *Q. J. R. Meteorol. Soc.*, *131*(612), 2961–3012, doi:10.1256/qj.04.176.

van Loon, H., and R. L. Jenne (1972), The zonal harmonic standing waves in the Southern Hemisphere, *J. Geophys. Res.*, *77*(6), 992–1003, doi:10.1029/JC077i006p00992.

Webster, P. J., A. M. Moore, J. P. Loschnigg, and R. R. Leben (1999), Coupled ocean-atmosphere dynamics in the Indian Ocean during 1997-98, *Nature*, *401*, 356–360, doi:10.1038/43848.

Wentz, F. J., L. Ricciardulli, K. Hilburn, and C. Mears (2007), How much more rain will global warming bring?, *Science*, *317*(5835), 233–235, doi:10.1126/science.1140746.

World Bank Group (2016), Global Economic Prospects, January 2016: Spillovers amid Weak Growth, Washington, DC, World Bank, Washington, D. C., doi:10.1596/978-1-4648-0675-9.

Yates, M. L., R. T. Guza, and W. C. O'Reilly (2009), Equilibrium shoreline response: Observations and modeling, *J. Geophys. Res.*, *114*, C09014, doi:10.1029/2009JC005359.

Young, I. R. (1999), Seasonal variability of the global ocean and wind and wave climate, *Int. J. Climatol.*, *19*(9), 931–950, doi:10.1002/(SICI)1097-0088(199907)19:9<931::AID-JOC412 > 3.0.CO;2-O.

Young, I. R., S. Zieger, and A. V. Babanin (2011), Response to comment on: "Global trends in wind speed and wave height", *Science*, *334*(6058), 905, doi:10.1126/science.1210548.

Young, I. R., J. Vinoth, S. Zieger, and A. V. Babanin (2012), Investigation of trends in extreme value wave height and wind speed, *J. Geophys. Res.*, *117*, C00J06, doi:10.1029/2011JC007753.

Yuan, J., and J. Cao (2013), North Indian Ocean tropical cyclone activities influenced by the Indian Ocean Dipole mode, *Sci. China Earth Sci.*, *56*(5), 855–865, doi:10.1007/s11430-012-4559-0.

Yuan, X., and C. Li (2008), Climate modes in southern high latitudes and their impacts on Antarctic sea ice, *J. Geophys. Res.*, *113*, C06S91, doi:10.1029/2006JC004067.

Zhang, Y., J. M. Wallace, and D. S. Battisti (1997), ENSO-like interdecadal variability: 1900-93, *J. Clim.*, *10*(5), 1004–1020, doi:10.1175/1520-0442(1997)010<1004:ELIV>2.0.CO;2.